RESEARCH ARTICLE

Key Points:
- Full-3-D tomography for Southern California crust
- Based on a combination of the SI and AW methods
- About half-a-million data were used

Correspondence to:
P. Chen,
pchen@uwyo.edu

Full-3-D tomography for crustal structure in Southern California based on the scattering-integral and the adjoint-wavefield methods

En-Jui Lee[1,2], Po Chen[1], Thomas H. Jordan[2], Phillip B. Maechling[2], Marine A. M. Denolle[3,4], and Gregory C. Beroza[3]

[1]Department of Geology and Geophysics, University of Wyoming, Laramie, Wyoming, USA, [2]Southern California Earthquake Center, University of Southern California, Los Angeles, California, USA, [3]Department of Geophysics, Stanford University, Stanford, California, USA, [4]Scripps Institution of Oceanography, University of California, San Diego, La Jolla, California, USA

Abstract We have successfully applied full-3-D tomography (F3DT) based on a combination of the scattering-integral method (SI-F3DT) and the adjoint-wavefield method (AW-F3DT) to iteratively improve a 3-D starting model, the Southern California Earthquake Center (SCEC) Community Velocity Model version 4.0 (CVM-S4). In F3DT, the sensitivity (Fréchet) kernels are computed using numerical solutions of the 3-D elastodynamic equation and the nonlinearity of the structural inversion problem is accounted for through an iterative tomographic navigation process. More than half-a-million misfit measurements made on about 38,000 earthquake seismograms and 12,000 ambient-noise correlagrams have been assimilated into our inversion. After 26 F3DT iterations, synthetic seismograms computed using our latest model, CVM-S4.26, show substantially better fit to observed seismograms at frequencies below 0.2 Hz than those computed using our 3-D starting model CVM-S4 and the other SCEC CVM, CVM-H11.9, which was improved through 16 iterations of AW-F3DT. CVM-S4.26 has revealed strong crustal heterogeneities throughout Southern California, some of which are completely missing in CVM-S4 and CVM-H11.9 but exist in models obtained from previous crustal-scale 2-D active-source refraction tomography models. At shallow depths, our model shows strong correlation with sedimentary basins and reveals velocity contrasts across major mapped strike-slip and dip-slip faults. At middle to lower crustal depths, structural features in our model may provide new insights into regional tectonics. When combined with physics-based seismic hazard analysis tools, we expect our model to provide more accurate estimates of seismic hazards in Southern California.

1. Introduction

Seismic waveforms generated by natural sources and recorded by modern seismometers carry rich information about Earth's internal structure. The latest tool for assimilating this information into seismic velocity models is fully three-dimensional (3-D) waveform tomography [e.g., *Tarantola*, 1988; *Tromp et al.*, 2005; *Chen et al.*, 2007a, 2007b; *Ben Hadj Ali et al.*, 2009a, 2009b; *Chen*, 2011; *Fichtner*, 2011; *Lekic and Romanowicz*, 2011; *Liu and Gu*, 2012; *Colli et al.*, 2013; *Fichtner et al.*, 2013; *French et al.*, 2013; *Prieux et al.*, 2013; *Schiemenz and Igel*, 2013]. Full-3-D tomography (F3DT) accounts for the physics of wave excitation and propagation by numerically solving the inhomogeneous equations of motion for a heterogeneous, anelastic solid [*Olsen et al.*, 1995; *Komatitsch and Tromp*, 1999; *Cui et al.*, 2010; *Peter et al.*, 2011]. The starting model is 3-D, and the Fréchet (sensitivity) kernels are calculated using the full physics of 3-D wave propagation [*Zhao et al.*, 2005, 2006; *Tromp et al.*, 2005; *Liu and Tromp*, 2006]. F3DT can employ any functional of the seismogram as observable, including frequency-dependent phase and group delays of earthquake waveforms [*Gee and Jordan*, 1992] and two-station correlagrams of the ambient seismic field [*Tromp et al.*, 2010; *Chen et al.*, 2010; *Xu et al.*, 2013]. F3DT accounts for the nonlinearity of the structural inverse problem through iterated cycles of forward simulation, data measurement, kernel calculation, and inversion.

Advances in high-performance computing have recently enabled the application of F3DT to large regional and global data sets [*Chen et al.*, 2007b; *Tape et al.*, 2010; *Zhu et al.*, 2012]. This paper describes how F3DT was used to assimilate more than a half-million measurements from earthquake waveforms and ambient-noise correlagrams to image the 3-D crustal structure of Southern California. We started with the Community Velocity Model of the Southern California Earthquake Center, version 4.0 (SCEC CVM-S4), and conducted 26

iterations using two complementary methods for F3DT inversion: the adjoint-wavefield (AW) technique [*Tarantola*, 1984, 1988; *Pratt*, 1990; *Pratt et al.*, 1998; *Akcelik et al.*, 2002, 2003; *Tromp et al.*, 2005; *Liu and Tromp*, 2006] and the scattering-integral (SI) technique [*Zhao and Jordan*, 1998; *Katzman et al.*, 1998; *Zhao et al.*, 2005, 2006; *Chen et al.*, 2007a, 2007b].

Though these methods are built on exactly the same physics, each has its own computational advantages and drawbacks [*Chen et al.*, 2007a]. Here we report how "tomographic navigation" through sequential inversion steps using both techniques can assimilate data sets of increasing precision and size. The result is CVM-S4.26, a 3-D velocity model with unprecedented resolution of the crustal features throughout Southern California.

Southern California is nearly ideal as a natural laboratory for constructing and validating F3DT models. More than 200 Myr of intense tectonic activity [*Burchfiel et al.*, 1992] has led to a highly heterogeneous crust. At shallow levels (≤2 km depth), the seismic velocities have been observed to vary by more than 50% [*Magistrale et al.*, 2000; *Süss and Shaw*, 2003]. The most extreme variations, in particular, the deep basins of low-velocity sediments, are controlled by active faulting. Many of the basin structures, especially in the Los Angeles region, are constrained by geological mapping, seismic activity, and the extensive sets of well logs and active-source surveys collected during petroleum exploration [*Süss and Shaw*, 2003; *Plesch et al.*, 2007]. Conformance to known shallow features provides a critical test of any velocity model, and it is an essential validation step for those intended for earthquake simulation.

A major goal of this study was to improve the accuracy of earthquake simulations for use in physics-based seismic hazard models [*Graves et al.*, 2010]. On the scale of Southern California, the overall fidelity of CVM-S4.26 to known crustal structure is significantly better than the CVM-S4 starting model and the other SCEC community velocity model, CVM-H11.9 [*Tape et al.*, 2009, 2010; *Plesch et al.*, 2011]. We also show that some peculiar features of the middle- and lower-crust, including interesting velocity reversals, are consistent with the limited structural samples provided by refraction seismology.

Small- to medium-sized earthquakes are common in Southern California. Since the mid-1980s, this seismicity has been recorded by broadband digital seismometers of Southern California Seismic Network (SCSN) [*Hauksson et al.*, 2001], which numbered more than 200 at the time of this study (Table A1), as well as occasional temporary seismographic deployments [e.g., *Gilbert et al.*, 2007]. Here we describe an iterated sequence of data measurements that targeted frequency-dependent phase and group delays of both earthquake waveforms and ambient-noise correlagrams. The data iteration features inversions for the centroid-moment tensors (CMTs) of the earthquake sources at various points in the velocity-structure iterations. In total, about 5,883,146 measurements were inverted through all iterations; the final (26th) structural inversion operated on 513,000 data points from 50,500 seismograms (Appendix A). This data set is comparable to the largest inverted in published global [e.g., *Kustowski et al.*, 2008] and regional [e.g., *Schaeffer and Lebedev*, 2014] tomographic studies. The source-receiver paths for earthquake and ambient-noise recordings are highly complementary, together providing a dense and fairly even coverage throughout the entire modeling domain (Figure 1).

2. SCEC Community Velocity Models of Southern California

Over the past 20 years, SCEC researchers have developed two 3-D "community" velocity models of Southern California, CVM-S and CVM-H. Each model has been refined through a series of releases. CVM-S was established by *Magistrale et al.* [2000], who embedded rule-based seismic velocity models of major Southern California basins, derived primarily from well log data [*Magistrale et al.*, 1996], within a background tomographic model constrained by regional traveltimes [*Hauksson*, 2000]. CVM-S was later improved by adding a high-resolution "geotechnical layer," a laterally varying Moho depth determined from receiver functions [*Zhu and Kanamori*, 2000], and an upper mantle seismic velocity model [*Kohler et al.*, 2003]. The latest version, which revised structures for the Salton Trough and San Bernardino Valley, was released as CVM-S4.

The CVM-H series has been developed primarily by researchers from Harvard University, beginning with *Süss and Shaw* [2003]. They determined basin structures from an extensive set of sonic logs and seismic reflection profiles collected by the petroleum industry, which they also embedded within *Hauksson*'s [2000] tomographic model. The latest version, CVM-H11.9.1, released in December 2012, includes a geotechnical layer based on shear velocities averaged over the upper 30 m (V_{S30}) [*Ely et al.*, 2010], a Moho interface by
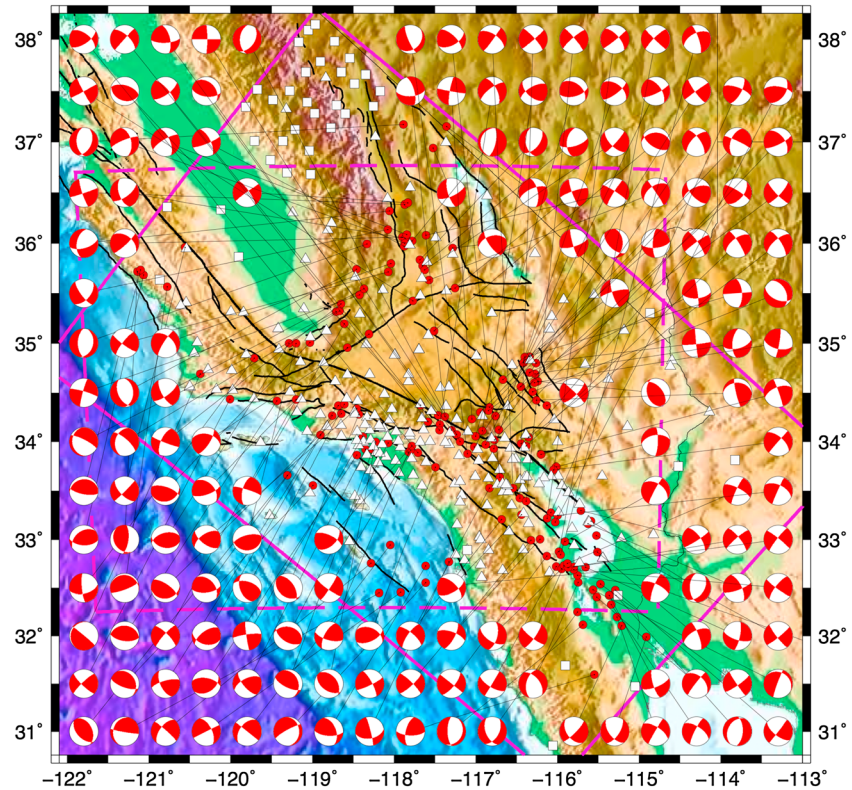
Figure 1. Distributions of the 160 earthquakes and 258 seismic stations used in this study. Red circles: epicenters of the earthquakes; beach balls: focal mechanisms of the earthquakes; white triangles: permanent broadband stations; white squares: temporary broadband stations; solid line magenta box: region of our F3DT study; dash line magenta box: region of the adjoint tomography conducted in *Tape et al.* [2009, 2010]; background color: regional topography; black solid lines: major faults.

Yan and Clayton [2007], and an upper mantle structure from finite-frequency teleseismic surface-wave tomography [*Prindle and Tanimoto*, 2006]. Notably, CVM-H11.9.1 incorporated the crustal structure obtained by *Tape et al.* [2009, 2010] from 16 AW-F3DT iterations of low-frequency earthquake waveform data. The CVM-H series is the velocity model native to SCEC's Unified Structural Representation, which also comprises the SCEC Community Fault Model [*Plesch et al.*, 2007].

The initial application of F3DT to the Los Angeles region [*Chen et al.*, 2007b] showed that synthetic seismograms computed using either CVM-S or CVM-H provided substantially better fits to observed seismograms than synthetics computed using either a 1-D regional velocity model [e.g., *Hadley and Kanamori*, 1977] or sets of path-averaged 1-D models. Synthetics computed using the inverted model, LAF3D, provided substantially better fit to observed waveforms than those computed using the 3-D starting model, CVM-S, and the inversion brought the Los Angeles Basin structure more into agreement with that in CVM-H.

In this study, we initiated our F3DT iterations using CVM-S4 as a starting model, which we represented on a regular grid with 500 m node spacing. We updated the two Lamé parameters in each iteration. The density model and the Moho depth were not perturbed during the iterations, and the anelastic attenuation was not included. Solutions of the 3-D inhomogeneous wave equation were obtained using the fourth-order, staggered-grid, finite-difference code developed by *Olsen* [1994], *Olsen et al.* [1995], *Marcinkovich and Olsen* [2003], and *Cui et al.* [2009]. The details of our wave-equation solver are documented in Appendix B.

3. F3DT Formulation

In full-3-D tomography (F3DT), information from a collection of observed seismograms $\mathbf{u}_{obs}$ is assimilated into a discretized structural model $\mathbf{m}$ through a finite series of finite perturbations:

$$\mathbf{m}_{k+1} = \mathbf{m}_k + \Delta\mathbf{m}_k, k = 0, 1, 2, \ldots, K. \qquad (1)$$

During the kth iteration, we use the best available model $\mathbf{m}_k$ to calculate synthetic seismograms $\mathbf{u}_k$, and we characterize the differences between $\mathbf{u}_{\text{obs}}$ and $\mathbf{u}_k$ by a set of differential waveform measurements $\mathbf{d}_k = \mathbf{d}$ ($\mathbf{u}_{\text{obs}}, \mathbf{u}_k$). The components of $\mathbf{d}$ are generally nonlinear functionals of the seismograms, such as the frequency-dependent phase and group delays of body waves and surface waves [*Gee and Jordan*, 1992; *Lee and Chen*, 2013]. Because multiple measurements are typically made on several waveforms per seismogram, $\mathbf{d}_k$ is much larger than $\mathbf{u}_k$, and its size increases with k as more measurements are included in the inverted data set.

The model perturbation $\Delta\mathbf{m}_k$ is constructed by minimizing a quadratic objective function that measures the waveform misfit relative to a positive-definite data covariance matrix $\mathbf{C}_d$ plus the perturbation size relative to a positive-definite model covariance matrix $\mathbf{C}_m$:

$$\chi^2(\mathbf{m}, \mathbf{m}_k) = \mathbf{d}^T(\mathbf{m}, \mathbf{m}_k)\mathbf{C}_d^{-1}\mathbf{d}(\mathbf{m}, \mathbf{m}_k) + (\mathbf{m} - \mathbf{m}_k)^T\mathbf{C}_m^{-1}(\mathbf{m} - \mathbf{m}_k). \tag{2}$$

Here the data are written as functionals of the approximate model $\mathbf{m}_k$ and the target model $\mathbf{m}$, which we take to be the data-generating model for $\mathbf{u}_{\text{obs}}$ (or, more precisely, the best representation of the data-generating model within the considered model space). We can expand this objective function about $\mathbf{m}_k$ using the Jacobian $\mathbf{A}_k = \partial\mathbf{d}_k/\partial\mathbf{m}_k$, i.e., the matrix whose rows are the discretized Fréchet derivatives of the data functionals with respect to the model. To second order, the results are

$$\chi^2(\mathbf{m}, \mathbf{m}_k) \simeq \chi_k^2 + \mathbf{a}_k(\mathbf{m} - \mathbf{m}_k) + \frac{1}{2}(\mathbf{m} - \mathbf{m}_k)^T\mathbf{H}_k(\mathbf{m} - \mathbf{m}_k). \tag{3}$$

The constant $\chi_k^2 = \chi^2(\mathbf{m}_k, \mathbf{m}_k)$ vanishes if $\mathbf{d}(\mathbf{m}_k, \mathbf{m}_k) = 0$. The linear and quadratic terms are given in terms of the data-weighted Fréchet kernel:

$$\mathbf{a}_k \equiv \nabla_{\mathbf{m}_k}\chi^2(\mathbf{m}, \mathbf{m}_k) = -\mathbf{A}_k^T\mathbf{C}_d^{-1}\mathbf{d}(\mathbf{m}, \mathbf{m}_k) \tag{4}$$

and the Hessian

$$\mathbf{H}_k \equiv \nabla_{\mathbf{m}_k}\nabla_{\mathbf{m}_k}\chi^2(\mathbf{m}, \mathbf{m}_k) = \mathbf{A}_k^T\mathbf{C}_d^{-1}\mathbf{A}_k + \mathbf{C}_m^{-1} + (\nabla_{\mathbf{m}_k}\mathbf{A}_k)^T\mathbf{C}_d^{-1}\mathbf{d}(\mathbf{m}, \mathbf{m}_k). \tag{5}$$

In the adjoint-wavefield implementation of full-3-D tomography (AW-F3DT), we solve for the data-weighted Fréchet kernel by integrating the seismic wavefield against an adjoint wavefield. The adjoint source used in this back propagation is obtained by replacing the data functional vector $\mathbf{d}(\mathbf{m}, \mathbf{m}_k)$ with its observed value $\mathbf{d}_k$ [*Tarantola*, 1988; *Akcelik et al.*, 2003; *Tromp et al.*, 2005]. We then follow *Tromp et al.* [2005] and estimate $\Delta\mathbf{m}_k$ by a conjugate-gradient method.

In the scattering-integral implementation (SI-F3DT), we calculate the full Jacobian $\mathbf{A}_k$ and approximate the Hessian by neglecting its third term. We minimize the objective function by setting its gradient with respect to the target model $\mathbf{m}$ equal to zero:

$$\nabla_{\mathbf{m}}\chi^2(\mathbf{m}, \mathbf{m}_k) = \mathbf{a}_k + \mathbf{H}_k(\mathbf{m} - \mathbf{m}_k) = 0. \tag{6}$$

Substituting $\mathbf{d}_k$ for $\mathbf{d}(\mathbf{m}, \mathbf{m}_k)$ leads to an equation for the model perturbation:

$$\left(\mathbf{A}_k^T\mathbf{C}_d^{-1}\mathbf{A}_k + \mathbf{C}_m^{-1}\right)\Delta\mathbf{m}_k = \mathbf{A}_k^T\mathbf{C}_d^{-1}\mathbf{d}_k. \tag{7}$$

The solution to this equation can be obtained from the equivalent linear system:

$$\begin{bmatrix} \mathbf{C}_d^{-1/2}\mathbf{A}_k \\ \mathbf{C}_m^{-1/2} \end{bmatrix}\Delta\mathbf{m}_k = \begin{bmatrix} \mathbf{C}_d^{-1/2}\mathbf{d}_k \\ 0 \end{bmatrix} \tag{8}$$

using an efficient, parallelized version of the LSQR algorithm [*Lee et al.*, 2013].

The computational costs of the AW-F3DT and SI-F3DT algorithms have been compared in *Chen et al.* [2007a]. Per iteration, AW-F3DT is usually more computationally efficient when the number of receivers is much larger than the number of sources. The disk storage costs of AW-F3DT, as well as the associated input/output (I/O) overhead, are usually small. Per iteration, SI-F3DT is usually more computationally efficient when the number of sources is comparable to or larger than the number of receivers. The disk and I/O costs of SI-F3DT are typically much higher than those of AW-F3DT, although they are now affordable with the high storage capacity and I/O speed of modern supercomputers. The peak disk storage during our SI-F3DT iterations in our Southern California modeling was about 39 Tb.

The key advantage of SI-F3DT is its rapid convergence rate, which can approach quadratic when the Hessian is dominated by the first term in equation (5) and the iteration scheme becomes approximately Newton [*Chen et al.*, 2007a]. In comparison, the conjugate-gradient iteration scheme of AW-F3DT converges only linearly and thus typically requires many more iterations to reach an optimal solution [*Nocedal and Wright*, 2006]. The details of our computational implementation are described in Appendix C.

4. Tomographic Navigation

F3DT is a nonlinear, iterative inversion process that requires hands-on navigation through the model space in order to reach a near-optimal structural model. This tomographic navigation process can be controlled through careful conditioning of the waveform data, the appropriate choice of different types of misfit measurements, and the proper choice of the AW or SI method. The majority of the seismograms used in our Southern California study came from SCSN recordings of local small- to medium-sized earthquakes. Errors in the CMTs used in computing synthetic seismograms can bias the waveform data. Therefore, at various stages in the tomographic navigation, we inverted the waveform data for the CMTs of the earthquakes used in subsequent iterations. The tomographic navigation that produced CVM-S4.26 is summarized in Figure 2.

4.1. Choice of Tomographic Method

At each iteration, we based our choice of the SI or the AW method on a qualitative assessment of their relative convergence rates and computational costs. The Hessian approximation can be poor when the starting model is far removed from the optimal model. In such situations, the convergence rate of the SI algorithm approaches that of the AW algorithm, and the gain from constructing the approximate Hessian may not justify its computational costs. For this reason, we used the AW method in most of the earlier iterations (Figure 2). An exception was our application of the SI method in the first two iterations, when the number of data was small and the computational cost was low.

As we improved the structural model, the synthetic seismograms were capable of fitting more of the observed waveforms, and we were able to increase the number and quality of the inverted data. At iteration 21, we switched from the AW method to the SI method, which accelerated the convergence rate by a factor of about 16 (i.e., the misfit reduction increased by 16 times compared with the previous iteration) (Figure 2). This increased the peak disk storage from about 200 Gb to about 39 Tb, which was mainly used for storing the source-side strain fields used in the SI method (Appendix C). In *Chen et al.* [2007b], the SI implementation was based on storing the receiver-side Green's tensors (RSGTs) [*Zhao et al.*, 2005, 2006]. In cases where the number of receivers is larger than the number of sources, storing the source-side strain fields instead of the RSGTs can significantly reduce storage costs.

4.2. Data Measurement and Inversion

We measured waveforms on two types of seismogram, SCSN recordings of regional earthquakes, ranging in moment magnitude from 3.3 to 5.7 in year 1998 to 2012, and two-station correlagrams obtained by cross correlating and stacking vertical component recordings of ambient noise at permanent and temporary seismic stations in Southern California. The initial screening and preprocessing of seismograms, as well as the ambient-noise stacking, are documented in Appendix A. The correlation of the ambient seismic field is known to be a reliable estimate of the surface-wave Green's function between two seismic stations [e.g., *Rickett and Claerbout*, 1999; *Lobkis and Weaver*, 2001; *Derode et al.*, 2003; *Weaver and Lobkis*, 2004; *Snieder*, 2004; *Wapenaar*, 2004; *Snieder et al.*, 2007]. In this study, we use the vertical-to-vertical component of the Green tensor, and we refer to them as ambient-noise Green's functions (ANGFs). The ambient seismic noise sources have to be uniformly or optimally oriented to guarantee accuracy of the amplitude and phase measurements. We use the processing described in *Prieto et al.* [2009] and *Lawrence and Prieto* [2011] that successfully retrieved phase and amplitude measurements for Southern California and the western U.S. In Southern California, the most energetic noise sources come form the Pacific Ocean [*Stehly et al.*, 2006], and we average the ANGFs causal and anticausal sides to reduce the directional source distribution effects. While numerical approaches predict large uncertainties in the retrieved estimates of the Green's function [*Tsai*, 2011; *Fichtner*, 2014], in practice, the effect of multiple scattering in crust improves that assumption of uniformity.

In the earlier iterations, we measured only waveforms corresponding to the main low-frequency seismic phases, i.e., *P* (or *Pnl*), *S*, and surface waves on the earthquake seismograms, and surface waves on the ambient-noise correlagrams. Other distinct waveforms were included in the later iterations; their Fréchet
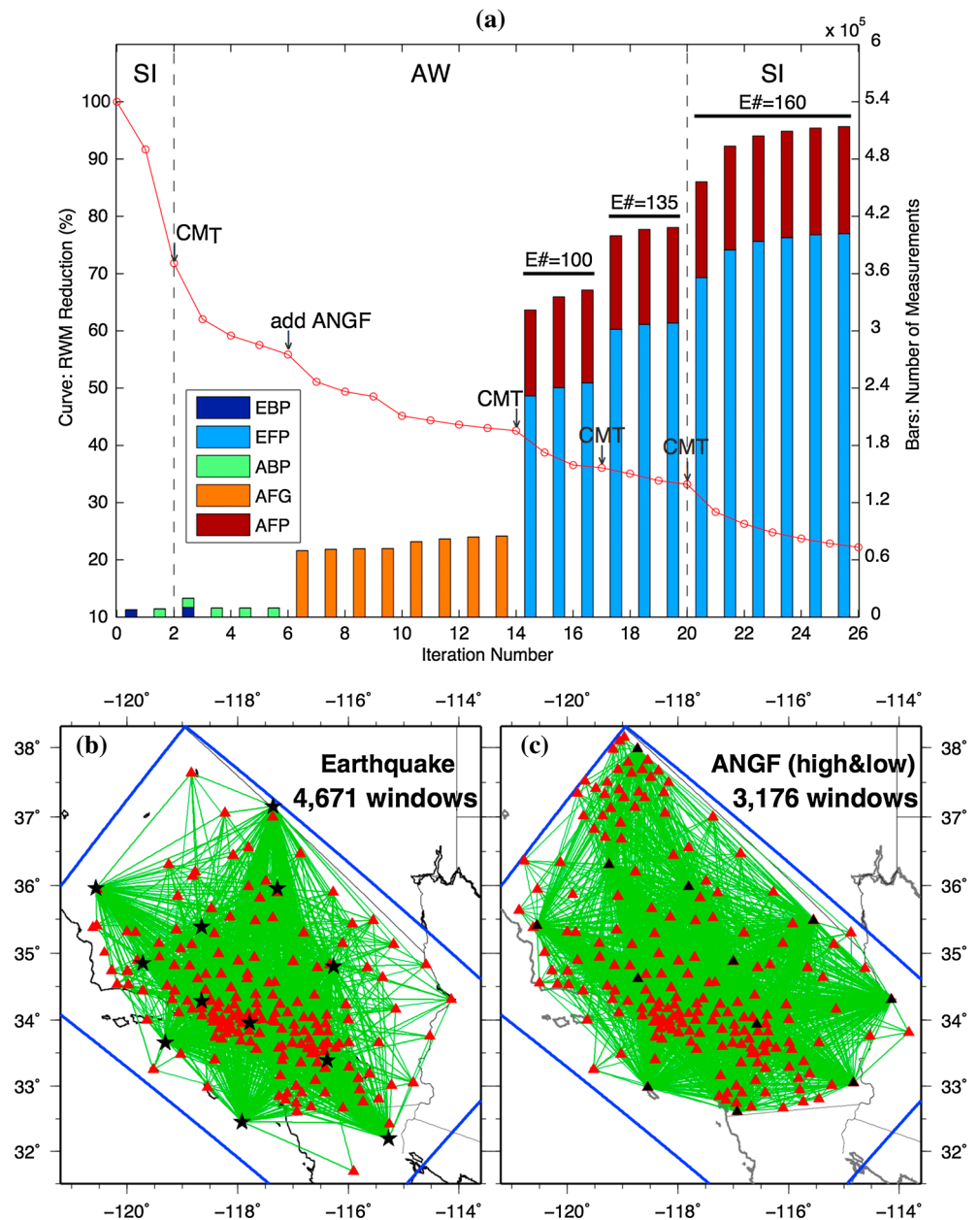
Figure 2. (a) Red solid line with circles: the relative waveform misfit (RWM) for a set of waveforms selected for monitoring the improvements of our model. Vertical bars: the number of misfit measurements used in each iteration. Colors of the vertical bars indicate the different types of the misfit measurements used. Vertical dash lines separate iterations carried out using the AW method from those carried out using the SI method. Black arrows indicate the iterations in which CMT inversions were performed or ambient-noise correlagrams were included. The number of earthquakes used in each iteration is shown following "E#=." (b) Source-receiver paths for the 4671 earthquake waveforms used for monitoring the RWM reduction. Black stars: earthquake epicenters; red triangles: broadband stations. (c) Interstation paths for the 3176 Rayleigh waves on the ambient-noise correlagrams (Appendix A) used for monitoring the RWM reduction. Black triangle: stations used as virtual sources; red triangles: stations used as receivers. The source-receiver paths for these selected waveforms are shown as green solid lines in Figures 2b and 2c.

kernels often exhibit complex 3-D wave propagation effects, such as multipathing and nongeometrical reflections and refractions.

Our data set comprised several types of data-synthetic phase misfits, which we measured using the generalized seismological data functional (GSDF) procedures described by *Gee and Jordan* [1992], *Chen et al.*

[2007b], and *Lee and Chen* [2013]. Each observed waveform was cross correlated with a synthetic waveform (isolation filter), windowed near zero lag, narrowband filtered, and fit with a Gaussian wavelet to obtain the frequency-dependent phase delays $\Delta T_p(\omega_k)$ and group delays $\Delta T_g(\omega_k)$. The measurements were typically made for a set of frequencies $\{\omega_k\}$ spaced at 0.01 Hz from 0.02 Hz to 0.20 Hz (Appendix A). For each waveform, we also measured the peak of the unfiltered cross-correlation function, which gives the "broadband" delay time ΔT_c, i.e., the phase delay of the observed waveform relative to the synthetic averaged across the full bandwidth of the waveform [*Sipkin and Jordan*, 1980; *Luo and Schuster*, 1991; *Tanimoto*, 1995; *Zhao and Jordan*, 1998; *Dahlen et al.*, 2000]. We calculated the Fréchet kernels for different measurement types using the appropriate seismogram perturbation kernels [*Chen et al.*, 2007a, 2007b, 2010], as described in Appendix D.

In earlier iterations, the synthetics were poorly aligned with the observed waveforms, especially in regions where the 3-D structure of the CVM-S4 starting model was relatively unconstrained (e.g., north and east of the Los Angeles region). We therefore found it more efficient to restrict the inverted data to the broadband delay times from the earthquake seismograms (earthquake broadband phase delays, abbreviated EBP) and ambient-noise correlagrams (ambient-noise broadband phase delays, abbreviated ABP). In iterations 7–14, we added sets of frequency-dependent group delays from the ambient-noise correlagrams (AFG). Beginning with iteration 15, after the large kinematic errors had been corrected, we switched to inverting much larger sets of earthquake frequency-dependent phase delays (EFP) and ambient-noise frequency-dependent phase delays (AFP). A noise model for the frequency-dependent phase delays is documented in Appendix E.

We also measured, but did not invert, the amplitudes of the observed waveforms relative to the synthetics, which we expressed as frequency-dependent amplitude-reduction times, $\Delta T_q(\omega_k)$ in the notation of *Gee and Jordan* [1992] and *Chen et al.* [2007b]. These measurements, along with the relative waveform misfit (RWM) (equation (9)) of the control data set shown in Figures 2b and 2c, were used to monitor improvements in the predicted waveforms.

4.3. CMT Inversions

The 160 earthquakes used in our study were well recorded by three-component broadband seismic stations of SCSN. The CMT solutions for the earthquakes were revised at selected iterations by applying the fast waveform-inversion technique of *Lee et al.* [2011]. Synthetic Green's functions were computed to 0.2 Hz from the updated crustal model by a reciprocity-based finite-difference method [*Zhao et al.*, 2006], and the optimal CMT parameters were found using a hierarchical grid-search algorithm that minimized the traveltime and amplitude differences for a selected set of observed waveforms. Figure 1 shows our revised locations and source mechanisms for all earthquakes used in our study.

In the earlier iterations, we mainly used ABP and AFG for improving the crustal model (Figure 2a). At iteration 15, CMT solutions for 100 earthquakes were revised using the updated crustal model, CVM-S4.14. EFP on the waveforms of these earthquakes were included to improve our crustal model in subsequent iterations. CMT revisions for 135 and 160 earthquakes were carried out at iteration 18 and 21 using CVM-S4.17 and CVM-S4.20, respectively. Our revised CMT solutions were generally consistent with the solutions provided by SCSN and provided better fit to the observed waveforms [*Lee et al.*, 2011].

5. Model Description

At shallow depths, CVM-S4.26 shows excellent correlation with surface geology. On the 2 km depth *S* wave velocity map (Figure 3a), the most significant low-velocity anomaly is associated with the Southern San Joaquin Basin (SSJB) [*Bailey et al.*, 1970; *Ingersoll*, 1982], which is mostly missing in both CVM-S4 and CVM-H11.9 but well imaged in our model. To the west of the SSJB, our model shows low-velocity anomalies associated with the Santa Maria Basin [e.g., *Hall*, 1991], the Cuyama Basin [e.g., *Davis et al.*, 1988], and an intermediate- to high-velocity anomaly associated with surface exposures of the Salinian basement rocks [e.g., *Jennings*, 1977; *Ducea et al.*, 2009]. To the east of the SSJB, our model shows a high-velocity belt in the western Sierra Nevada foothills, which is correlated with magnetic and gravity anomalies (Figure 3b). This high-velocity belt corresponds to a series of well-exposed ring-dike complexes, which appear to be the roots of Early Cretaceous basalt-andesite volcanic centers [*Mack et al.*, 1979; *Saleeby and Sharp*, 1980; *Clemens-Knott and Saleeby*, 1999; *Clemens-Knott et al.*, 2000]. To the east of the Sierra Nevada Fault zone, along the Owens
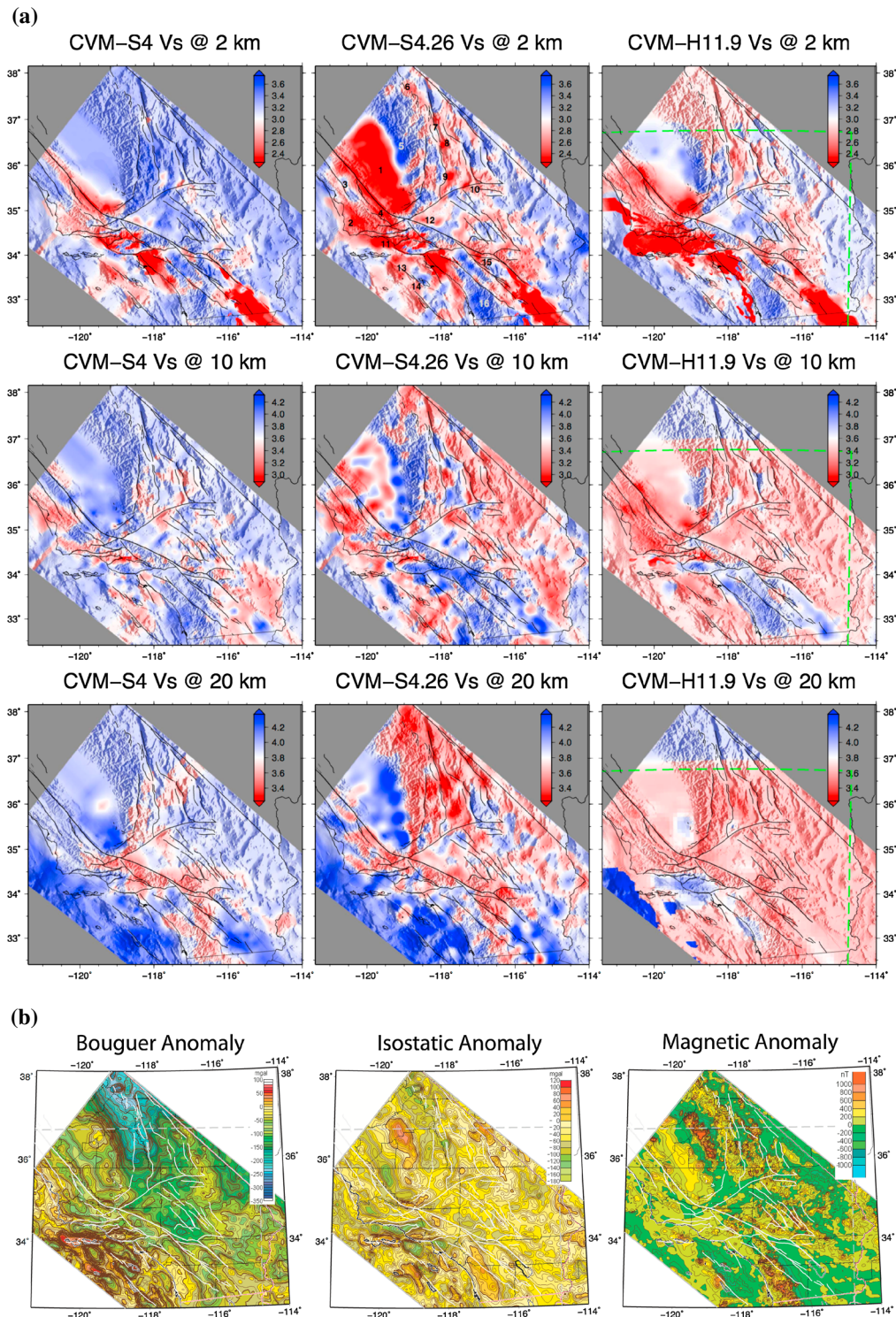
Figure 3. (a) *S* wave velocities at (top) 2 km, (middle) 10 km, and (bottom) 20 km depths in (left) CVM-S4, (middle) CVM-S4.26, and (right) CVM-H11.9. The color bar on the upper left corner of each plot shows the range of the color scale with red indicating relatively slow *S* wave velocities and blue indicating relatively fast *S* wave velocities. Green dash line boxes on right column indicate the tomography region of *Tape et al.* [2009, 2010]. Black solid lines show major faults in Southern California. Numbers shown in the top row, middle column indicate locations of some geological features. 1: Southern San Joaquin Basin (SSJB); 2: Santa Maria Basin; 3: Salinian basement outcrop; 4: Cuyama Basin; 5: Ring-dike complexes; 6: Long-Valley Caldera; 7: Big Pine Volcanic Field; 8: Owens Lake; 9: Indian Wells Valley (China Lake); 10: Searles Lake; 11: Santa Barbara Channel; 12: Antelope Valley; 13: Santa Monica Basin; 14: Catalina Schist outcrop; 15: San Bernardino Basin; 16: Peninsular Ranges Batholith. (b) Bouguer, isostatic, and magnetic anomaly maps within our tomography region. White solid lines show major faults. The gravity and magnetic data were downloaded from http://www.uwgb.edu/dutchs/StateGeophMaps/CalifGphMap.HTM.

Valley, our model shows a sequence of low-velocity anomalies associated with the Long-Valley Caldera, the Big Pine Volcanic Field, the Owens Lake, the Indian Well's Valley, and the Searles Lake. The Ventura Basin and the offshore Santa Barbara Channel both lie in a structural downwarp of a major fold-and-thrust belt [e.g., *Keller*, 1990], and our model shows that the low-velocity anomaly associated with the Ventura Basin in CVM-S4 has been extended offshore into the Santa Barbara Channel in CVM-S4.26 (Figure 3a). Our model also shows low-velocity anomalies associated with the offshore basins, such as in the Santa Monica Basin, the San Pedro Basin, the Catalina Basin, the Gulf of Catalina, and the San Diego Trough. The intermediate- to high-velocity anomaly on the Santa Catalina Island might be associated with the uplifted Catalina Schist [e.g., *Woodford*, 1924; *Bailey*, 1941; *Platt*, 1975; *Legg*, 1991]. In the Mojave Desert, our model shows lower velocities in the Antelope Valley than CVM-S4 and CVM-H11.9. The velocities in the San Bernardino Basin are also lower in our model than in CVM-S4 and CVM-H11.9. The high-velocity anomaly associated with the Peninsular Ranges Batholith is well correlated with magnetic and gravity anomalies (Figure 3b).

At middle to lower crustal depths, CVM-S4.26 reveals correlation with the different tectonic provinces in Southern California. The significant differences among different tectonic units can be seen on their laterally averaged velocity profiles (Figure 4). The averaged velocity profiles in SSJB (Figure 4a) show a relatively high velocity body right beneath the low-velocity basin, and this feature is also imaged by the active-source 2-D tomographic results (Figure 7) [*Fliedner et al.*, 2000] and might be interpreted as the Great Valley Ophiolite [e.g., *Godfrey and Klemperer*, 1998]. Beneath the eastern edge of the SSJB and the ring-dike complexes in the western Sierra Nevada foothills, a very high velocity volume ($Vs > 4.0$ km/s; $Vp > 7.0$ km/s) appear in the middle to lower crust (Figure 4b) and this feature is also consistent with the gravity and magnetic anomalies (Figure 3b). One possibility is that this high-velocity volume belongs to the western mafic part of the Sierra Nevada batholith of Early Cretaceous [*Saleeby et al.*, 2003]. In eastern Sierra Nevada (Figure 4c), the averaged velocity profiles show relatively low velocities ($Vs < 3.75$ km/s; $Vp < 6.5$ km/s) in middle to lower crust, which is consistent with a negative Bouguer gravity anomaly in this region (Figure 3b). In CVM-S4.26, the western (Figure 10) and the eastern Mojave (Figure 4d) separated by the Eastern California Shear Zone show very different velocity profiles, which is consistent with the Bouguer gravity anomalies in the Mojave regions (Figure 3b). The middle to lower crustal velocities in the eastern Peninsular Ranges (Figure 4e) are lower than those in the western Peninsular Ranges region (Figure 4f), which is correlated with the gravity and magnetic anomalies in this region (Figure 3b). A more detailed geological interpretation of our crustal model will be documented in a separate paper.

6. Model Assessment

In our tomographic navigation process, only phase misfits were inverted. However, synthetic seismograms computed using CVM-S4.26 show remarkable fit to both the phases and the amplitudes of observed waveforms. We measure the difference between the observed waveform $u_{obs}(t)$ and its corresponding synthetic waveform $u(t)$ within the time window $[t_k, t_k']$ using the relative waveform misfit (RWM) [e.g., *Zhu and Helmberger*, 1996]:

$$\text{RWM}_k = \frac{\int_{t_k}^{t_k'} [u_{obs}(t) - u(t)]^2 dt}{\sqrt{\int_{t_k}^{t_k'} [u_{obs}(t)]^2 dt \int_{t_k}^{t_k'} [u(t)]^2 dt}}, \tag{9}$$

where the time windows $[t_k, t_k']$ were those used in the 26th iteration. Roughly speaking, RWM < 1 indicates a good waveform fit, whereas RWM > 1 indicates a poor fit [*Lee et al.*, 2014]. We computed the RWMs for 43,496 earthquake waveforms, 10,853 Rayleigh waves on ANGF-high ambient-noise correlagrams, and 12,581 Rayleigh waves on ANGF-low ambient-noise correlagrams. We computed the average RWM at a station by averaging the RWM values over all (up to 3) components at that station, all earthquakes recorded by that station and all ambient-noise correlagrams involving that station. The maps shown in Figure 5 were obtained by interpolating the average RWMs at all the stations used in our study. Histograms of the RWMs for all earthquake seismograms, all ANGF-high, and all ANGF-low are plotted below the maps for each CVM. Labeled on each histogram are its median value (mRWM) and median absolute deviation (MAD), statistics that provide robust measures of the location and spread of a univariate distribution [*Hoaglin et al.*, 1983].
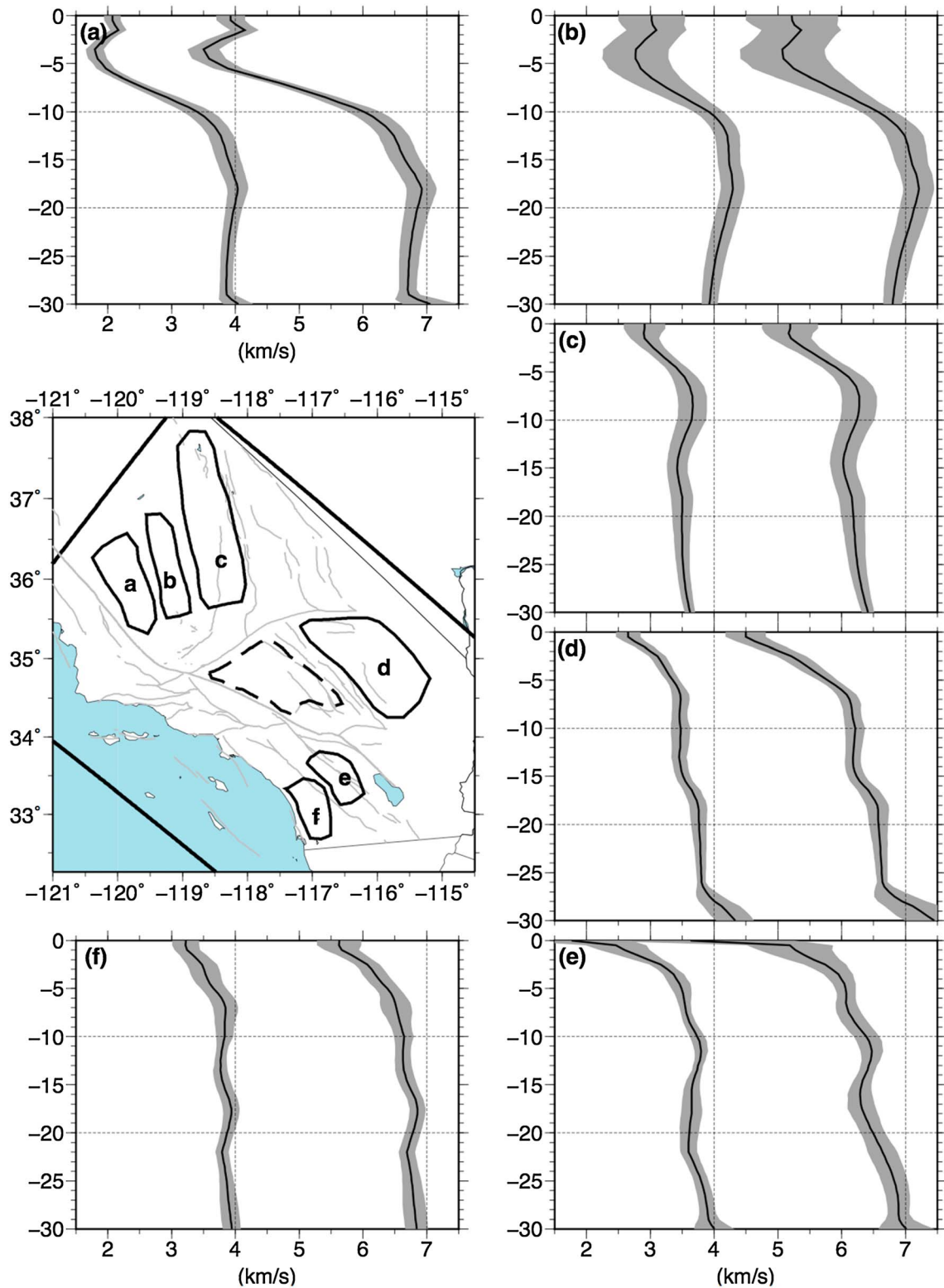
Figure 4. Laterally averaged velocity-depth profiles for different tectonic provinces in Southern California. The velocity profiles for western Mojave (dash line in the map) are shown in Figure 10. The velocity profiles for regions marked with letter "a" to "f" on the map are shown as black solid lines on the plots labeled with the same letters. The gray zones on the velocity profile plots show the ranges of one standard deviation.
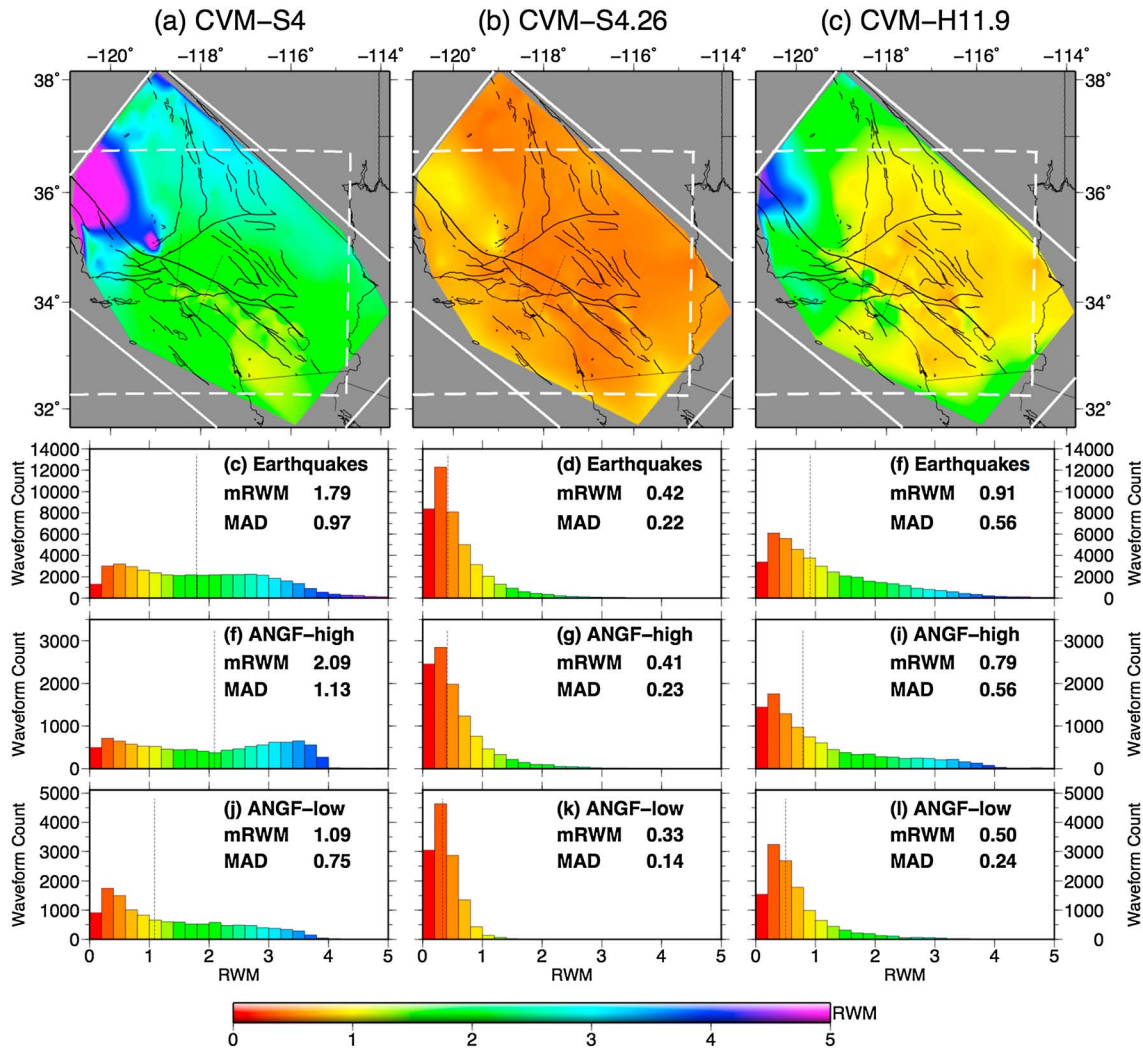
Figure 5. (a–c) The interpolated averaged RWM maps for CVM-S4, CVM-S4.26, and CVM-H11.9 and the histograms of the RWM for earthquake waveforms and for Rayleigh waves on ANGF-high and ANGF-low ambient-noise correlagrams. MAD: median absolute deviation; mRWM: median RWM. Warm colors indicate better fits. White solid line box: our tomography region; white dash line box: the tomography region of *Tape et al.* [2009, 2010].

Synthetics computed using CVM-S4.26 provide significantly better fit to all observed waveforms throughout the entire Southern California than synthetics computed using the other two CVMs. Synthetics computed using CVM-H11.9 provide better fits than those computed using CVM-S4. For all three CVMs, the fits to ANGF-low are better than the fits to ANGF-high and earthquake seismograms. Examples of observed and synthetic seismograms for selected source-receiver paths are shown in Figure 6. We point out several paths crossing major basins, such as those from 14095628 to SCZ2 and SDD, from 14155260 to STS, from 10215753 to CTC, and from 9854597 to SRN. For these paths, CVM-S4.26 provides substantially better fits than the other two models.

The complete inversion process is highly nonlinear, but within each iteration, we are solving a linearized problem, which allows us to use linear theory for model appraisal at the estimated model "locally." In Appendix F, we show checkerboard tests computed using the approximate Hessian of the 26th iteration. The results of the checkerboard tests show that the smallest scale that our 26th iteration can resolve is about 5 km. The highest resolution is around the center of our tomography region from about 1 km depth to about 25 km depth. However, we note that the results of the checkerboard tests may underestimate the resolution of the full nonlinear inversion because the nonlinear constraints imposed by the waveforms are usually much stronger than linear constraints imposed by the phases.
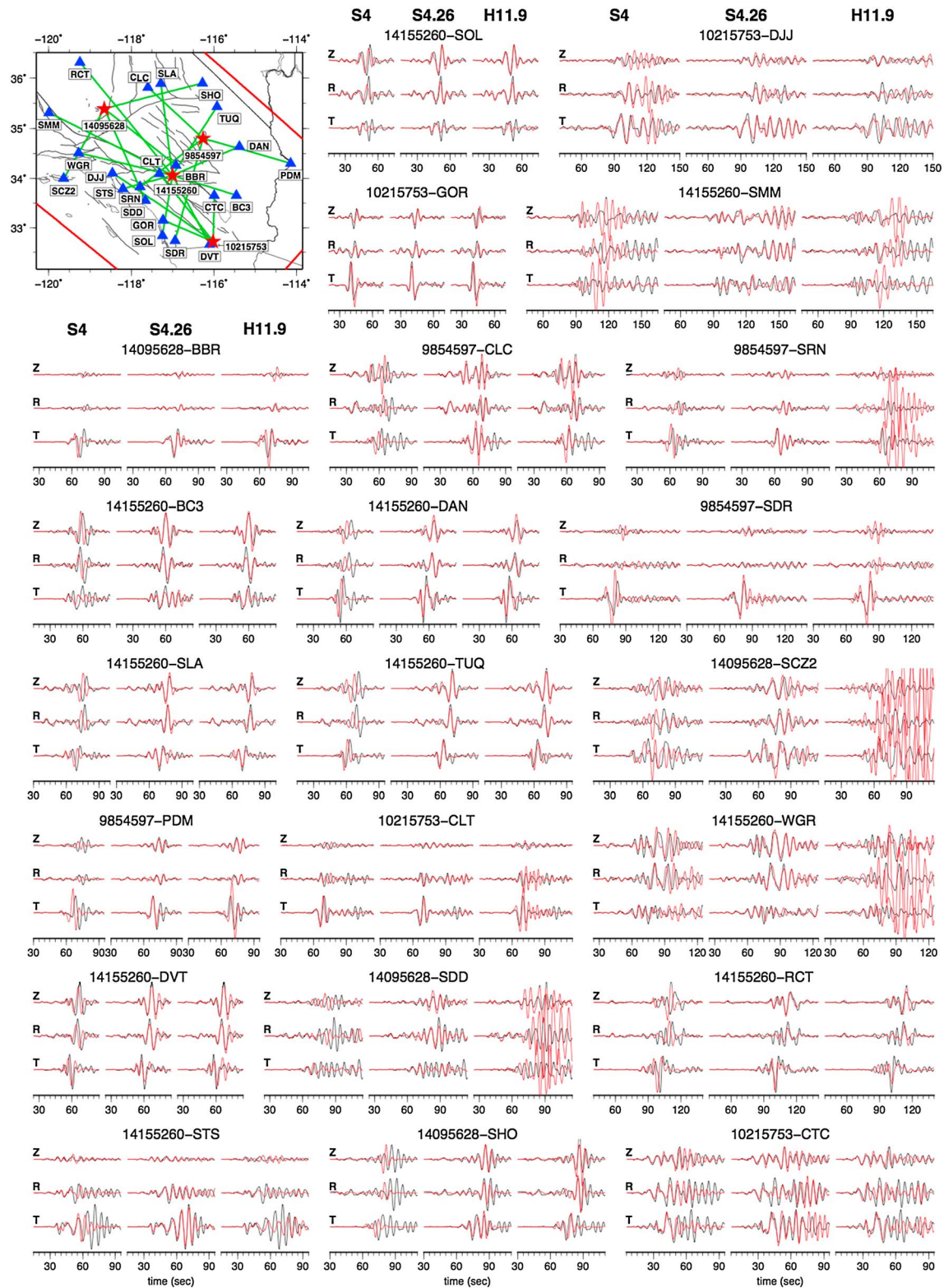
Figure 6. Examples of (top) vertical, (middle) radial, and (bottom) transverse component observed seismograms (black lines) and the corresponding synthetics (red lines) computed using (left) CVM-S4, (middle) CVM-S4.26, and (right) CVM-H11.9. The source-receiver paths for the selected waveform examples are shown in the upper left plot. Red stars: earthquake epicenters; blue triangles: receivers.

6.1. Comparisons With Active-Source Studies

A pragmatic approach for model assessment is to compare models obtained using different data sets and/or different methodologies. The agreement or disagreement among those models can be used to assess the reliabilities of different features in those models. Active-source studies usually have much higher data densities along survey profiles than our study. We can compare 2-D cross sections through the three CVMs with active-source 2-D tomography models. We have compared with 14 active-source 2-D refraction tomography models in Southern California. CVM-S4.26 has higher correlation coefficients than the other 2 CVMs for 10 out of the 14 refraction tomography models (Figures 7–9).

For crustal structure in the Coast Ranges, the SSJB, the Sierra Nevada, and the Basin and Ranges, we compare with the seven active-source tomography models published in *Fliedner et al.* [2000] (Figure 7). The low-velocity body associated with the SSJB extends down to about 8 km depth. A high-velocity body with maximum *P* wave velocity exceeding 7 km/s lies underneath most of the SSJB and the western Sierra Nevada foothills. In CVM-S4.26, the western part of this high-velocity body is about 5–10 km thick, and its eastern part is about 10–20 km thick. In the eastern Sierra Nevada, the *P* wave velocity at the middle and lower crustal depths in CVM-S4.26 is relatively low (~6 km/s or less), which is consistent with the findings in *Fliedner et al.* [2000].

In Figure 8, we compare 2-D cross sections through the three CVMs with the 2-D active-source refraction tomography models along the two profiles of the Los Angeles Region Seismic Experiments, LARSE-I [*Lutter et al.*, 1999] and LARSE-II [*Lutter et al.*, 2004]. Along the LARSE-I profile, underneath the San Gabriel Mountains (SGM), a low-velocity body extends down to 7 km depth in both CVM-S4.26 and *Lutter et al.* [1999]. In both models, an intermediate-velocity body (6–6.2 km/s) intrudes into the low-velocity body under the SGM along the Vincent Thrust Fault. To the southwest of the SGM a high-velocity body (6.5–7 km/s) lies underneath the San Gabriel Valley in both CVM-S4.26 and *Lutter et al.* [1999]. To the northeast of the SGM in the Mojave Desert, both models have low velocities and sharp velocity gradients at shallow depth (<2 km) and at about 6 km depth the *P* wave velocities in both models reach about 6.5 km/s.

Along the LARSE-II profile (Figure 8), the basin structures in *Lutter et al.* [2004] are much more consistent with those in CVM-S4.26 than those in the other two CVMs. Compared with CVM-S4, the thicknesses of the sedimentary basins in the San Fernando Valley and the Santa Clarita Valley are reduced in CVM-S4.26 and the intermediate-velocity body that separates the two basins is enhanced in CVM-S4.26. The velocities inside the Antelope Valley are reduced, and the low velocities associated with sediments at shallow depths are extended more to the north in CVM-S4.26. In CVM-H11.9, the San Fernando Valley and the Santa Clarita Valley are shown as a single large basin extending down to about 6–8 km depths; both the thickness and the shape of the basin are inconsistent with those in *Lutter et al.* [2004]. The *P* wave velocities inside the Antelope Valley are too high and the velocities beneath the Antelope Valley are too low in CVM-H11.9.

The Salton Seismic Imaging Project (SSIP) carried out in March 2011 had seven active-source profiles crossing different parts of the Salton Trough area [*Rose et al.*, 2013]. *Fuis et al.* [2012] have shown preliminary *P* wave velocity models for Lines 4, 5, and 6, *Livers et al.* [2012] have shown a model for Line 3, and *Han et al.* [2013] have shown a model for Line 1. Comparisons along these five SSIP lines are shown in Figure 9. Along Line 1, an intermediate-velocity layer with *P* wave velocity ranging from 6.5 km/s to 6.7 km/s lies under the sedimentary layer in both CVM-S4.26 and *Han et al.* [2013]. In CVM-S4 and CVM-H11.9, the velocities are too high under the Coachella Valley at 5–10 km depth. In *Han et al.* [2013], a northwest dipping reflector lies at about 20–23 km depth under the Coachella Valley, which may correspond to the sharp velocity gradient from about 6 km/s to 6.7 km/s at about the same location in CVM-S4.26. Lines 4, 5, and 6 are much shorter than Line 1, and resolutions of the three CVMs along these three lines are much lower than those in *Fuis et al.* [2012]. But in general, we observe better agreement in both the shape and the average velocities of the Coachella Valley between CVM-S4.26 and the active-source models. Along Lines 4 and 5, the asymmetry of the basin is consistent between CVM-S4.26 and *Fuis et al.* [2012]. Along Line 6, the lateral average velocities at shallow depths (<4 km) in CVM-S4.26 are more consistent with those in *Fuis et al.* [2012].

6.2. Conformance to Fault Structures

Our starting model CVM-S4 does not have faults explicitly built into the structural representation. However, we observe strong velocity contrasts across many mapped faults in CVM-S4.26. These cross-fault velocity
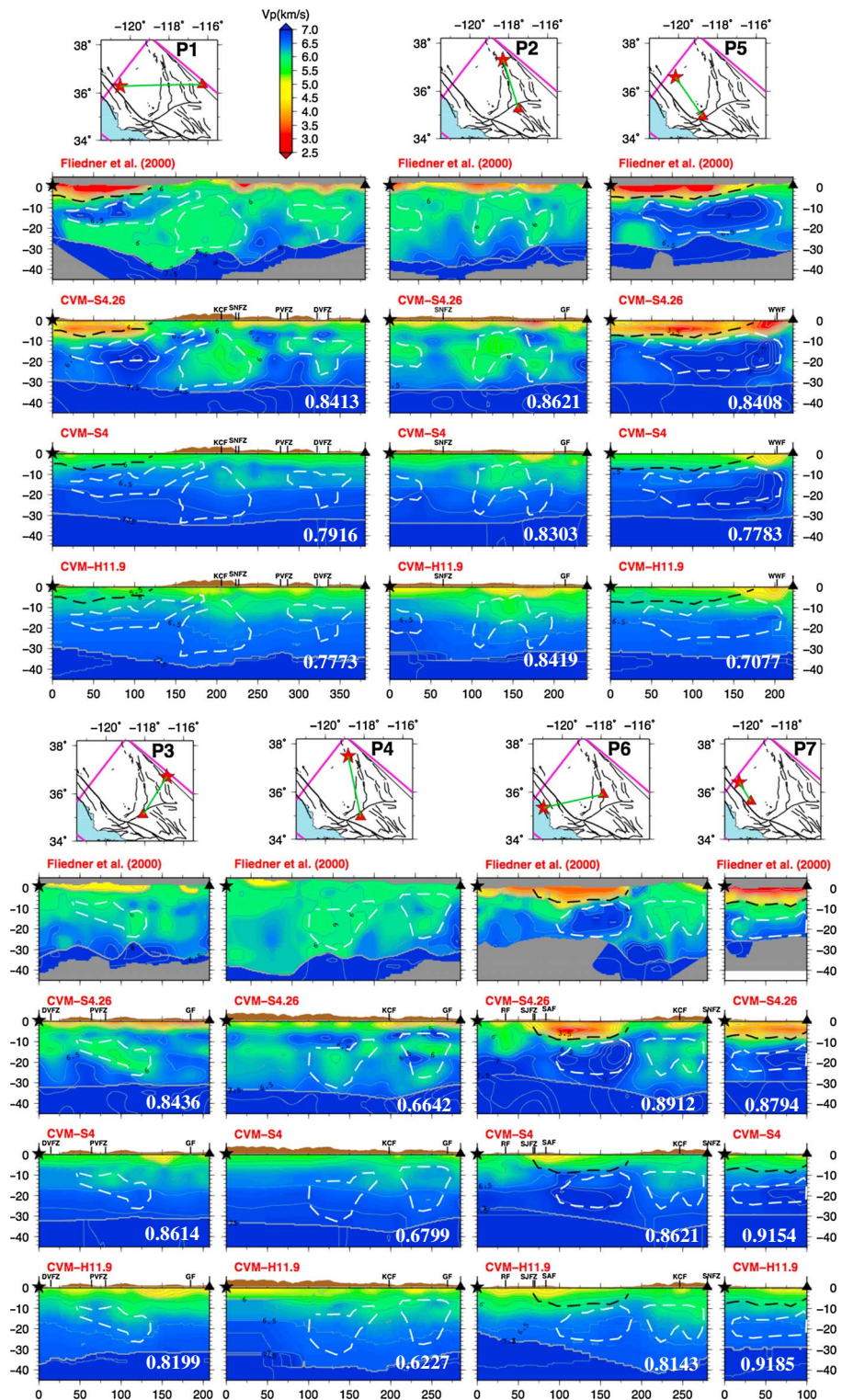
Figure 7. Cross sections of the *P* wave velocities in CVM-S4.26, CVM-S4, and CVM-H11.9 along the seven profiles shown in *Fliedner et al.* [2000]. We digitized and recolored the 2-D refraction tomography models shown in Plate 1 in *Fliedner et al.* [2000] using the same color scale as the 2-D cross sections of the CVMs with the permission from Simon Klemperer. Vertical exaggeration on the 2-D models and the cross sections is 2.5. Black and white dash lines in this figure and Figures 8 and 9 highlight some of the structural features in the active-source refraction tomography models and their corresponding positions in the cross sections of the three CVMs. The white boldface numbers on the cross sections of the CVMs show the correlation coefficients with the corresponding 2-D refraction tomography models.
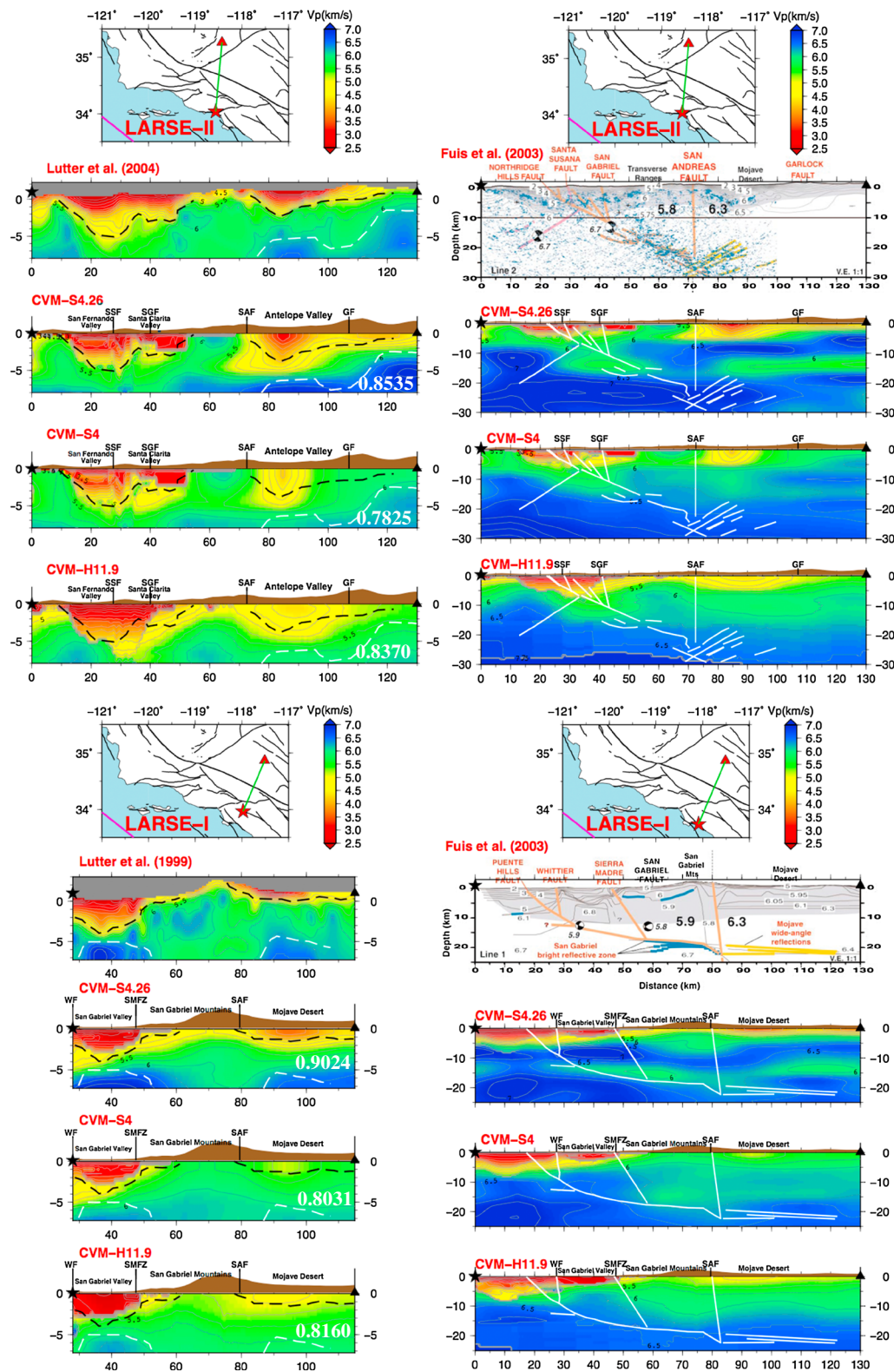
Figure 8. Cross sections of the *P* wave velocities in CVM-S4.26, CVM-S4, and CVM-H11.9 along the (top) LARSE-II line and the (bottom) LARSE-I line at (left) shallower and (right) larger depths. We digitized and recolored the 2-D tomography models of *Lutter et al.* [1999, 2004] with permission from Gary Fuis. The 2-D interpreted reflection profiles from *Fuis et al.* [2003] were reproduced with permission from Gary Fuis. White solid lines on the cross sections of the three CVMs show the locations of the interpreted faults in *Fuis et al.* [2003]. Vertical exaggeration is 2 on Figure 8 (left) and 1 on Figure 8 (right). The white boldface numbers on the cross sections of the CVMs show the correlation coefficients with the corresponding 2-D refraction tomography models.
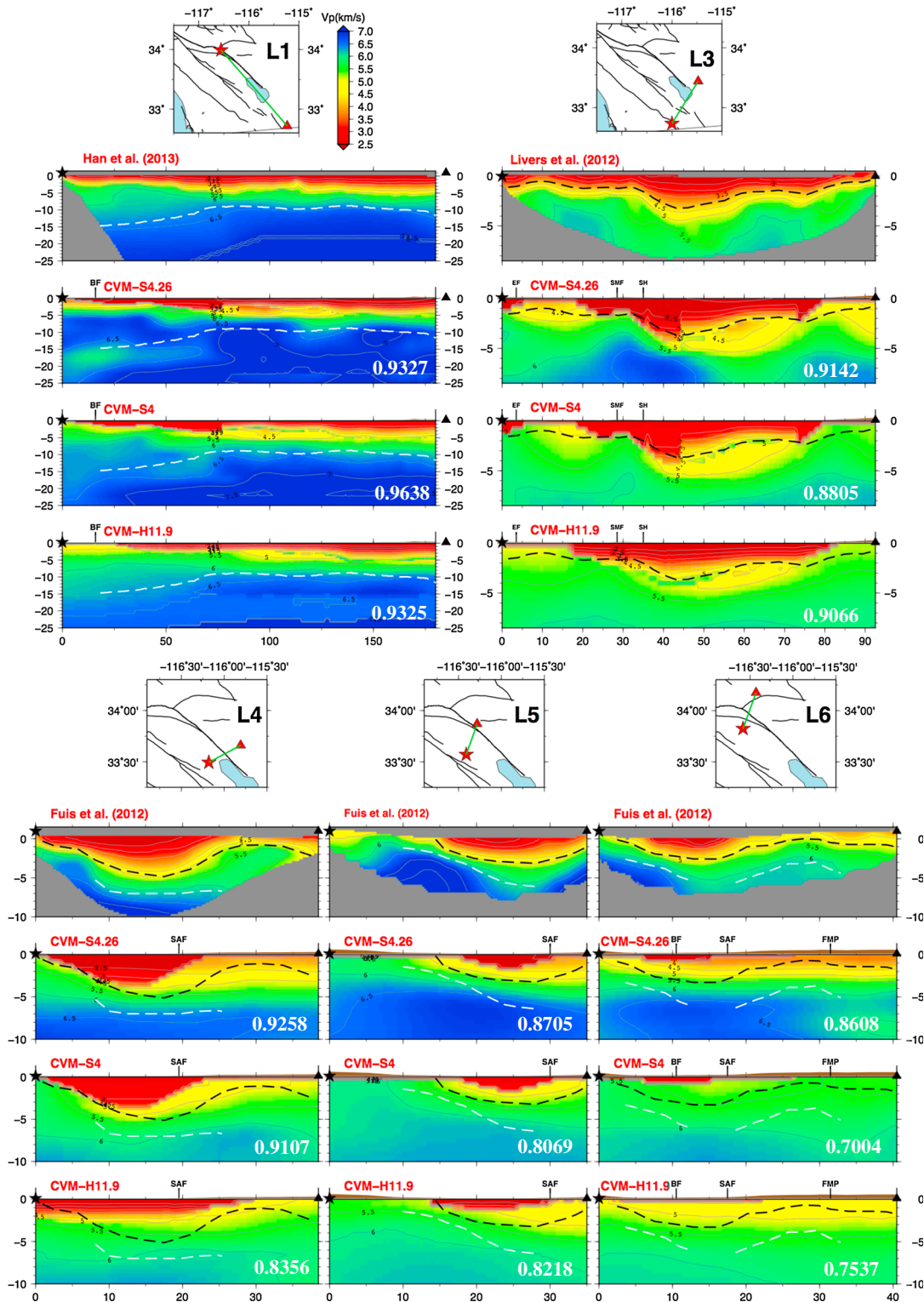
Figure 9. Cross sections of the *P* wave velocities in CVM-S4.26, CVM-S4, and CVM-H11.9 along five of the SSIP lines. We digitized and recolored the 2-D tomography models of *Fuis et al.* [2012], *Livers et al.* [2012], and *Han et al.* [2013] with the permission from Gary Fuis and John Hole. The vertical exaggeration is 2 for line L1 and 1 for other lines. The white boldface numbers on the cross sections of the CVMs show the correlation coefficients with the corresponding 2-D refraction tomography models.

variations introduced through our tomographic navigation process can serve as an independent verification of our model and also provide a rough estimate of the lower bounds of our model's resolution in some areas.

In CVM-S4.26, from 16 km to 24 km depth, the San Andreas Fault (SAF) is a sharp boundary between the relatively low velocities in the Salinian block and the intermediate to high velocities under the southern San Joaquin Basin (SSJB) (Figure 3a). This velocity contrast is shown as a bump on the 6.5 km/s contour on the cross-section view in P6, Figure 7. In about the same depth range, there is also a velocity reduction of about 5%–10% from the Mojave block to the San Gabriel block across the SAF (Figure 3a).

In CVM-S4.26, we can see velocity contrasts across the Garlock Fault (GF) at nearly all depth ranges (Figure 3a). At 2–4 km depths, the GF separates the high velocities in the Tehachapi Mountains from the low velocities in the Antelope Valley and the intermediate velocities in the western Mojave Desert. From 10 to 16 km, the velocities in the Tehachapi Mountains are nearly 20% lower than those in the western Mojave. Within the same depth range, the velocities in the Indian Wells Valley north of the GF are about 20% higher than those in the Rand Mountains south of the GF. Further to the east, the velocities in the Searles Lake, the Slate Range, and the Panamint Range to the north of the GF are about 15% lower than those in the Granite Mountains south of the GF.

At 2 km depth, the Sierra Nevada Fault Zone separates the high velocities in the Sierra Nevada from the low velocities in the Owens Valley (Figure 3a). The velocity contrast across the Kern Canyon Fault (KCF) can be seen at 6–12 km depths and on average the velocities west of the KCF are higher than those east of it. The velocity contrasts across the Eastern California Shear Zone are evident at upper and middle crustal depths. The San Gabriel-Sierra Madre-Cucamonga Faults (SGSMCF) forms the southwestern boundary of the San Gabriel block, and the velocity contrasts across SGSMCF can be seen at most depth ranges. At 2 km depth, the northern segment of the San Jacinto Fault, also known as the Claremont Fault, separates the low velocities in the San Bernardino Basin from the high velocities in the Peninsular Ranges. At the same depth, south of the Temecula Elsinore, the Elsinore Fault separates the high velocities in the southwest from the intermediate to low velocities in the northeast.

Along the LARSE-II profile, we see a low-velocity wedge lies under the San Fernando Valley from about 6 km depth to about 19 km depth in CVM-S4.26 (Figure 8). High-velocity bodies lie on both sides of the low-velocity wedge. The velocity contrasts along the south and the north sides of the low-velocity wedge are aligned with projections of the Northridge Thrust Fault and the San Fernando Thrust Fault on the LARSE-II profile [*Carena and Suppe*, 2002; *Fuis et al.*, 2003].

7. Discussion

CVM-S4.26 reveals strong crustal heterogeneities throughout Southern California. The interpretations for many of the structural features in this model, especially at middle to lower crustal depths, are still uncertain. For instance, in CVM-S4.26, there exists a pervasive low-velocity layer at about 12–17 km depth under most of the Western Mojave, the San Gabriel, the Southernmost Sierra Nevada, and the Salinian block. We laterally averaged the *P* and *S* wave velocities and the Poisson's ratio in Western Mojave to obtain the averaged velocity-depth and Poisson's ratio-depth profiles. Both the averaged *P* and *S* wave velocities show a low-velocity layer with about 11% maximum reduction at 12–17 km depth, and the averaged Poisson's ratio has about 8% maximum increase within the same depth range (Figure 10). This middle crustal low-velocity layer is visible on the cross sections along the LARSE-I and -II profiles (Figure 8). It is also seen along a longer profile from the receiver function study of *Porter et al.* [2011] (Figure 10). One possible interpretation is that this low-velocity layer corresponds to the underplated schists derived from the adjacent accretionary trench complex during the Laramide shallow flat subduction and later uplifted to middle crustal depths and partially exhumed during the post Laramide extensional collapse of the crust [e.g., *Saleeby*, 2003; *Ducea et al.*, 2009]. More in-depth studies on such issues should take into account laboratory measurements of the relevant types of rocks at various pressure and temperature conditions [e.g., *Christensen and Mooney*, 1995; *Pellerin and Christensen*, 1998] and also regional tectonics [e.g., *Ernst*, 1981], which are beyond the scope of this paper.

The SSJB, which is mostly missing in our starting model CVM-S4, has been reconstructed in CVM-S4.26 (Figure 3a) through our F3DT, and our inverted basin structure is in broad agreement with external constraints, such as sonic logs and industrial seismic reflection/refraction data, not included in our inversion (A. Plesch, personal communications, 2014). The accumulative velocity perturbation inside the SSJB through
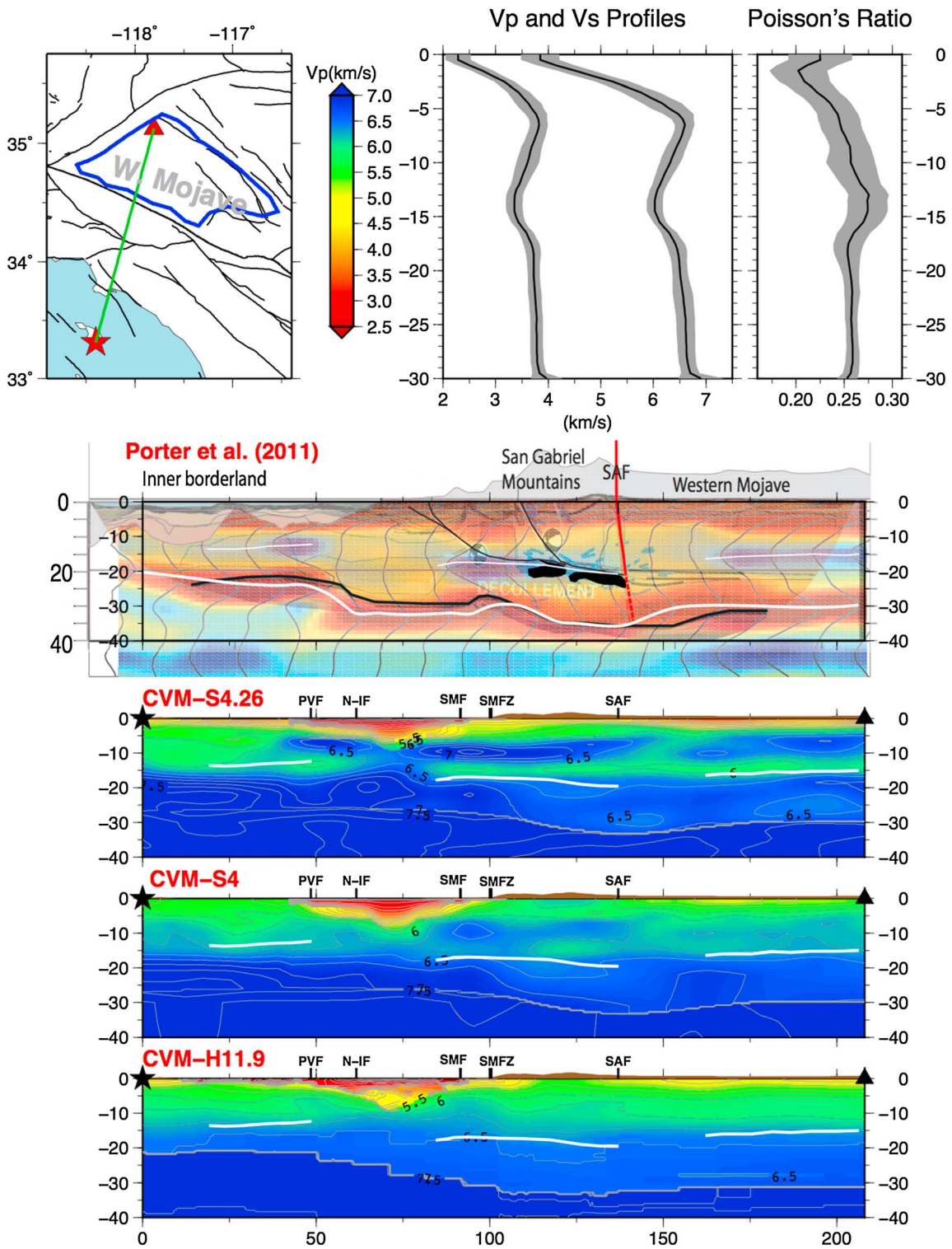
Figure 10. Blue solid line in upper left plot: the western Mojave region in which the laterally averaged velocities and Poisson's ratio were obtained. Black solid lines in upper right plots: the laterally averaged depth-dependent *P* and *S* wave velocities and the Poisson's ratio for the western Mojave region. The grey zones on both sides of the black solid lines show the ranges of 1 standard deviation. The figure of receiver function stack is from *Porter et al.* [2011] with permission from Ryan Porter. The three thin white lines in *Porter et al.* [2011] show the middle crustal low-velocity zone. These three white lines are duplicated at the same locations on the 2-D cross sections of the three CVMs. We note that in *Porter et al.* [2011], a *P* wave velocity of 6.4 km/s and a *Vp/Vs* ratio of 1.75 were used to convert the time axis to the depth axis.

the 26 iterations was over 60%, which suggests that our iterative tomographic navigation process can effectively account for the nonlinearity in structural inverse problems. The number of earthquake seismograms in and around the SSJB is much lower than in the rest of the Southern California. Our basin structure is therefore mostly constrained by ambient-noise correlagrams for stations pairs crossing the SSJB. The Fréchet kernels of the ambient-noise correlagram between two stations were computed by assuming a spatially Dirac virtual source located at one of the stations [*Chen et al.*, 2010; *Xu et al.*, 2013]. For uneven distributions of noise sources, the virtual source at one of the stations is usually smeared in both space and time and the algorithm that accounts for this smearing in the Fréchet kernels is given in *Tromp et al.* [2010]. In this study we did not adopt this algorithm for the following reasons:

1. The computational cost of this algorithm is significantly higher.
2. This algorithm requires a noise source distribution, which is usually unknown, and errors in the assumed noise source distribution can still introduce errors into the kernels.
3. Previous studies have shown that the phase measurements of the ambient-noise correlagrams in Southern California are relatively robust [e.g., *Ma et al.*, 2008].
4. For inversions that involve a large number of kernels, errors in individual kernels are likely to be averaged out during the inversion process.

The fact that we were able to reconstruct the SSJB in our inversion by using mostly ambient-noise correlagrams contributes another evidence that ambient-noise correlagrams can be used to improve the structure model in F3DT, complementary to earthquake seismograms.

From iteration 20 to 21, we switched from AW-F3DT to SI-F3DT and the convergence rate increased by a factor of about 16 (Figure 2). We attribute this increase in the convergence rate to the use of the approximate Hessian in SI-F3DT. In *Chen et al.* [2007a], we estimated that six–seven AW iterations based on the conjugate-gradient (CG) algorithm could match one SI iteration based on the Gauss-Newton (GN) algorithm. For the 2-D numerical experiment carried out in *Tape et al.* [2007], it took seven CG-based AW iterations to match one GN iteration. Results from this study have shown that for realistic complex 3-D structure models, the number of CG-based AW iterations required to match one GN-based SI iteration is significantly higher than the previous estimates in *Chen et al.* [2007a] and *Tape et al.* [2007]. The computational efficiency of SI-F3DT depends very much upon the efficiency of the LSQR code used for solving equation (8). In the 26th iteration, our linear system has over 38 million columns and over 261 million rows. The total number of nonzero elements in the matrix is over 144 billion. We have redesigned the parallel implementation of the LSQR algorithm to solve such large linear systems efficiently on distributed-memory parallel computer clusters [*Lee et al.*, 2013]. Our optimized LSQR code was able to complete 300 LSQR iterations within 5 min of wall time on 11,200 CPU cores, which is nearly 2 orders of magnitude faster than the LSQR code in the PETSc library [*Balay et al.*, 1997].

8. Conclusions

We have successfully applied both AW-F3DT and SI-F3DT to iteratively improve the SCEC CVM-S4 through a hands-on tomographic navigation process. The resulting model, CVM-S4.26, reveals strong crustal heterogeneities throughout Southern California. At shallow depths, CVM-S4.26 shows excellent correlation with surface geology and conformance to mapped fault structures. At middle to lower crustal depths, CVM-S4.26 has high correlations with 2-D refraction tomography models obtained from past active-source seismic surveys. Synthetic seismograms computed using CVM-S4.26 show remarkable fit to an extensive data set, including over 38,000 earthquake seismograms and over 12,000 ambient-noise correlagrams, at frequencies up to 0.2 Hz. In a companion paper, *Lee et al.* [2014], we tested the waveform prediction capability of CVM-S4, CVM-S4.26, and CVM-H11.9 by comparing synthetic seismograms computed using the three CVMs with over 900 seismograms recorded from two recent Los Angeles earthquakes, the 17 March 2014 Encino earthquake (M_W4.4) and the 29 March 2014 La Habra earthquake (M_W5.1). Seismograms from these two recent earthquakes were not used in deriving the three CVMs; therefore, they provide prospective tests of the models' forecasting skill. In general, synthetics computed using CVM-S4.26 provide substantially better fit to observed seismograms at frequencies below 0.2 Hz than those computed using the other two CVMs. Efforts are currently underway to extend the same F3DT process to the statewide California and also to further improve the accuracy of our crustal model by assimilating observed waveforms at higher frequencies. We are also extending our F3DT methodology and software to include intrinsic attenuation and anisotropy. We expect our crustal model to be

Table A1. Seismic Networks and the Number of Broadband Stations in Each Network Used in This Study

Network ID	Network Name	Data Source	Station Number
AZ	ANZA Regional Network	SCEDC	17
BK	Berkeley Digital Seismic Network (BDSN)	SCEDC	2
CI	Caltech/USGS Regional Seismic Network	SCEDC	199
NR; RB	NARS-Baja Network	SCEDC	4
TA	USArray Transportable Array	SCEDC	12
XE	Sierra Nevada EarthScope Flex Array	IRIS	24

useful for a wide variety of applications in California, including long-term seismic hazard assessment and earthquake early warning.

Appendix A: Seismogram Processing

Earthquake seismograms were collected from 258 three-component, broadband stations in seven different seismic networks (Figure 1 and Table A1). The majority of those seismograms were downloaded from the Southern California Earthquake Data Center (SCEDC), and seismograms from temporary seismographic deployments were downloaded from the Data Management Center (DMC) of Incorporated Research Institutions for Seismology (IRIS). Horizontal component seismograms were rotated into the radial and transverse components, and a very small number of seismograms were rejected during this process because of the two horizontal components not being orthogonal to each other during the recording of some earthquakes. The mean and the linear trend of each seismogram were removed, and a Hanning taper was applied. We then filtered each seismogram using a band-pass Butterworth filter with corners at 50 s and 5 s periods. The filtered seismograms were checked for signal-to-noise (SNR) ratio. We used two types of SNR definitions:

$$\text{SNR}_E = E_S/E_N = \frac{\displaystyle\int_{t_S^0}^{t_S^1}[u_{\text{obs}}(t)]^2\,\mathrm{d}t/\left(t_S^1 - t_S^0\right)}{\displaystyle\int_{t_N^0}^{t_N^1}[u_{\text{obs}}(t)]^2\,\mathrm{d}t/\left(t_N^1 - t_N^0\right)},$$

$$\text{SNR}_A = A_S^{\max}/A_N^{\max},$$

where $u_{\text{obs}}(t)$ is the observed seismogram, $\left[t_N^0, t_N^1\right]$ and $\left[t_S^0, t_S^1\right]$ are time windows containing the background noise and the seismic signal, and $A_N^{\max}$ and $A_S^{\max}$ are the maximum amplitudes of the noise and the seismic signal. We used a segment of the seismogram before the estimated first arrival time as the noise window. We rejected the seismograms with either SNR_E or SNR_A less than 3. A very small number of seismograms were also rejected because of instrument problems related to polarity reversals and gain corrections, which were easily detected by comparing with seismograms from neighboring stations during our CMT inversion stage [*Lee et al.*, 2011]. The number of earthquake seismograms increased through our tomographic navigation process and reached 38,069 by the 26th iteration (Table A2).

The ambient-noise correlagrams were obtained through the procedure documented in *Prieto et al.* [2011]. Only Rayleigh waves on vertical component correlagrams were used in our inversion. The amplitude spectrums of the ambient-noise correlagrams usually show two peaks at around 0.065 Hz and 0.14 Hz associated with the primary and the secondary microseisms
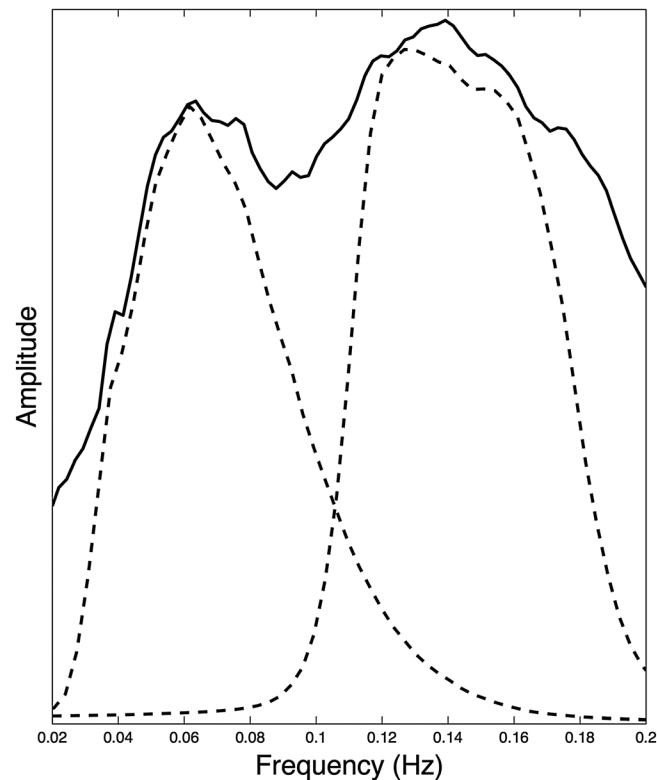
Table A2. The Number of Different Types of Seismograms, Waveforms, and GSDF Phase-Delay Measurements Used in the 26th Iteration

Seismograms	
Earthquake seismograms	38,069
ANGF-h	10,853
ANGF-l	12,581
Total	61,503
Waveforms	
Earthquake waveforms	43,496
ANGF-h waveforms	10,853
ANGF-l waveforms	12,581
Total	66,930
GSDF Phase Delays	
Earthquake measurements	401,838
ANGF-h measurements	61,939
ANGF-l measurements	50,090
Total	513,867

LEE ET AL.   6440

Figure A1. Black solid line: the averaged amplitude spectrum of all ambient-noise correlagrams used in this study; black dash lines: the amplitude spectrums filtered using the two Butterworth band-pass filters.

(Figure A1). To isolate the two microseism sources, we applied two band-pass Butterworth filters on each ambient-noise correlagram, one with corners at 33.33 s and 10 s periods and the other with corners at 9 s and 5.56 s periods (Figure A1), and obtained two filtered ambient-noise correlagrams, which we call "ANGF-low" (i.e., filtered with the lower pass band) and "ANGF-high" (i.e., filtered with the higher pass band). The filtered ambient-noise correlagrams were checked for SNR, and we rejected those with SNR_E or SNR_A less than 3. In the 26th iteration, we used 12,581 ANGF-low and 10,852 ANGF-high ambient-noise correlagrams (Table A2).

The selected earthquake seismograms and ambient-noise correlagrams were compared with the corresponding synthetic seismograms, and misfit measurements were made on selected waveforms. The waveforms used for making misfit measurements were selected in each iteration using a semiautomatic algorithm documented in *Lee and Chen* [2013]. The total number of waveforms used in the last iteration was 66,930 (Table A2). The frequency-dependent GSDF measurements [*Gee and Jordan*, 1992] were made on the selected waveforms. An example of the GSDF analysis on an earthquake waveform used in this study is shown in Figure A2. In the last iteration, we inverted 513,867 frequency-dependent GSDF phase-delay measurements, among which about 22% were measured on ambient-noise correlagrams (Figure A3).

Appendix B: Wave-Equation Solver

Our wave-equation solver is the Anelastic Wave Propagation (AWP-ODC) code [*Olsen*, 1994; *Cui et al.*, 2009], which solves the 3-D (visco)elastic wave equation using the fourth-order, staggered-grid finite-difference method. It implements the perfectly matched layer for absorbing boundaries [*Marcinkovich and Olsen*, 2003] and has been parallelized using the message passing interface. The simulation volume is 900 km long, 450 km wide, and 50 km deep (Figure 1). It is discretized into a uniform mesh with 500 m grid spacing, and the total number of grid points is about 162 million. For the maximum frequency of the synthetic seismograms at 0.2 Hz, we have nine grid points per minimum wavelength. For the fourth-order finite-difference scheme adopted in AWP-ODC, four–five grid points per minimum wavelength are usually sufficient for modeling body waves accurately and eight–10 grid points per minimum wavelength are sufficient for modeling surface waves accurately. The maximum *P* wave velocity inside our simulation volume is around 8200 m/s. Considering the Courant-Friedrichs-Lewy stability condition, we use a time step length of 0.03 s in our simulations. The length of the synthetic seismograms is 180 s, and the total number of time steps is 6000. On the IBM Blue Gene/Q system, each simulation uses 2048 cores for about 15 min of wall time.

In the modeling region, spherical coordinates were converted to Cartesian coordinates using the universal transverse Mercator projection. For the longest source-receiver distance involved in our inversion, which was about 606 km, the distortion in distance caused by our coordinate conversion was less than 0.2%. According to the Earth-flattening transformation [*Aki and Richards*, 2002], the depth-dependent velocity bias caused by our coordinate conversion should be about 0.5% at 30 km depth.
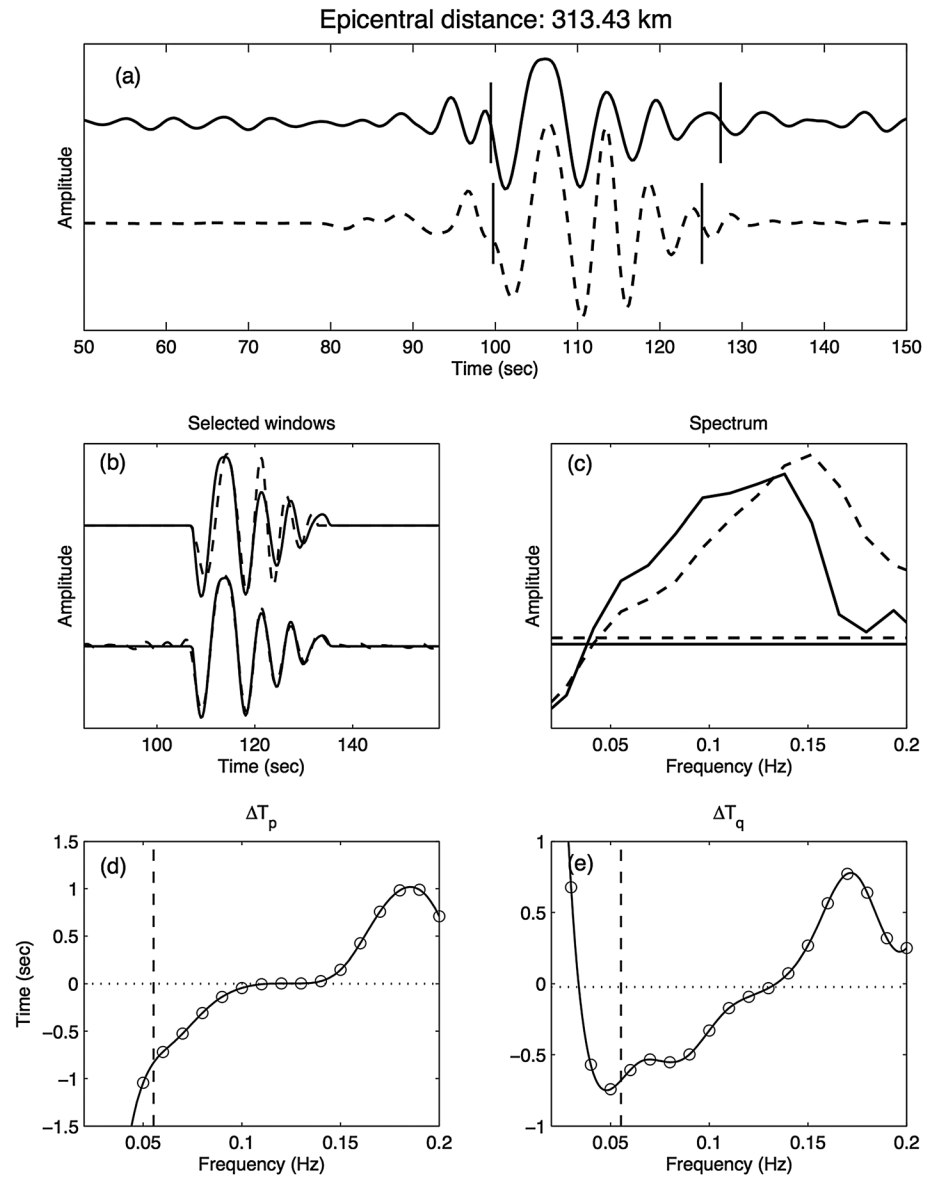
Figure A2. An example of measuring frequency-dependent GSDF phase delay and amplitude-reduction times on an earthquake waveform. (a) Observed (solid line) and synthetic (dash line) seismograms; (b) The top traces show the target observed waveform (solid line) and the selected synthetic waveform (isolation filter) (dash line); the bottom traces show the fit between the observed waveform (solid line) and the synthetic waveform (dash line) corrected using the frequency-dependent phase and amplitude misfit measurements shown in Figures A2d and A2e. (c) The amplitude spectrums of the observed (solid line) and synthetic (dash line) waveforms, the horizontal solid and dash lines indicate 33% of the peak amplitudes of the observed and synthetic waveforms, respectively. (d) Frequency-dependent phase delay of the observed waveform relative to the synthetic waveform (solid line), horizontal dotted line indicates the broadband cross-correlation phase delay, outside the vertical dash line the amplitude of the synthetic or the observed waveform falls below 33% of the peak amplitudes. (e) Frequency-dependent amplitude-reduction times, the horizontal dotted line indicates the natural log of the broadband cross-correlation amplitude ratio, the vertical dash line has the same meaning as in Figure A2d.

Appendix C: Computational Cost

For the 18 AW iterations we have carried out so far, the forward and the adjoint strain fields for each earthquake source, or virtual source in the case of ambient-noise correlagrams, were both computed using the AWP-ODC code. For each source, the forward simulation was carried out first and the synthetic seismograms and the forward strain fields were stored on disk. The misfit measurements were made using
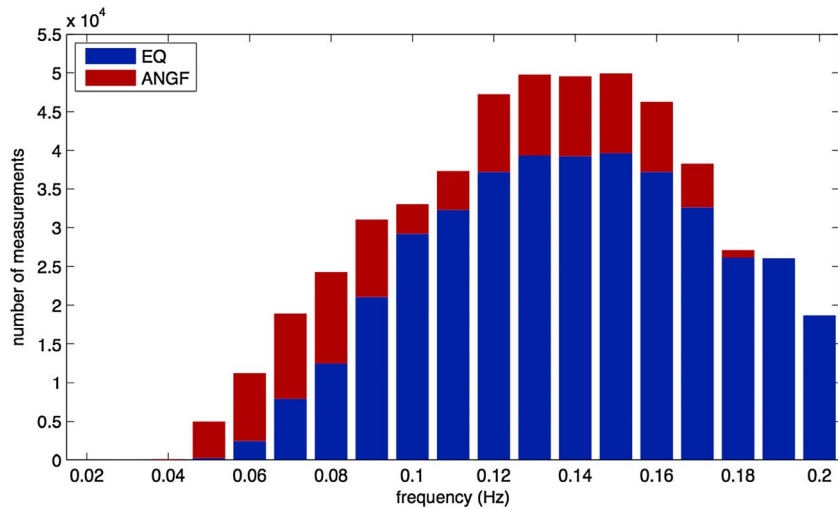
Figure A3. Distribution of all GSDF phase delays for the last iteration at different frequencies for both earthquake waveforms and Rayleigh waves on ambient-noise correlagrams.

those synthetics, and the adjoint source field was constructed. Then we ran the adjoint simulation using the adjoint source field as the source. After all time steps were completed in the adjoint simulation, the forward strain fields were read back from the disk, reversed in time, and the zero-lag temporal correlation with the adjoint field was computed at every spatial grid point. The resulting "adjoint kernel" was written to disk and the forward strain fields for this source were deleted from disk.

The strain fields were decimated by a factor of 2 in each spatial dimension and a factor of 10 in the time dimension before they were written to disk. The highest frequency in the simulations was 0.2 Hz. A decimation factor of 10 in time gave a temporal sampling interval of 0.3 s, which amounted to about 17 points per minimum period and was sufficient for avoiding temporal aliasing effects. The adjoint kernel was usually much smoother than the oscillatory wave fields, and a decimation factor of 2 in each spatial dimension did not introduce any spatial aliasing effects. The disk space for storing the decimated strain fields of one source was about 200 Gb.

The adjoint kernel was preconditioned based on the geometric spreading factor, a technique similar to that in *Fichtner et al.* [2009], to reduce the excessively large sensitivities in the vicinities of the sources and receivers. The summation of all adjoint kernels gave the gradient of the objective function. The gradient was then smoothed by convolving with a three-dimensional spatial Gaussian function [*Tape et al.*, 2007, 2010]. The horizontal width and the vertical width of the Gaussian function were chosen separately to maximize the reduction of the objective function in that iteration. The descent direction was computed using the smoothed gradient according to Fletcher-Reeves' conjugate-gradient algorithm [*Press et al.*, 1992]. A line search was then performed along the descent direction using a quadratic interpolation method [e.g., *Tromp et al.*, 2005; *Tape et al.*, 2007].

In the SI iterations, both the source-side strain fields and the receiver-side strain Green tensors (RSGTs) [*Zhao et al.*, 2005, 2006] were computed using the AWP-ODC code. The strain fields were decimated by a factor of 2 in each spatial dimension and a factor of 10 in time. For ambient-noise correlagrams, the receivers were also virtual sources. Since we were using only the vertical component correlagrams in our inversion, only one finite-difference simulation with a vertical point force at the virtual source location was needed for each virtual source. For all ambient-noise correlagrams used in our inversion, the total amount of disk space needed to store the strain fields for about 200 virtual sources was about 39 Tb. Once all the strain fields were obtained, the data sensitivity kernels for all misfits measured on ambient-noise correlagrams were computed using the scattering-integral method [*Zhao et al.*, 2005, 2006; *Chen et al.*, 2010]. The strain fields were all deleted from the disk after the data sensitivity kernels for all ambient-noise correlagrams were obtained.

For the 160 earthquakes used in our inversion, we stored all the source-side strain fields on disk, which occupied about 31 Tb disk space. The RSGTs were not written to disk. Once a RSGT was computed, it was kept
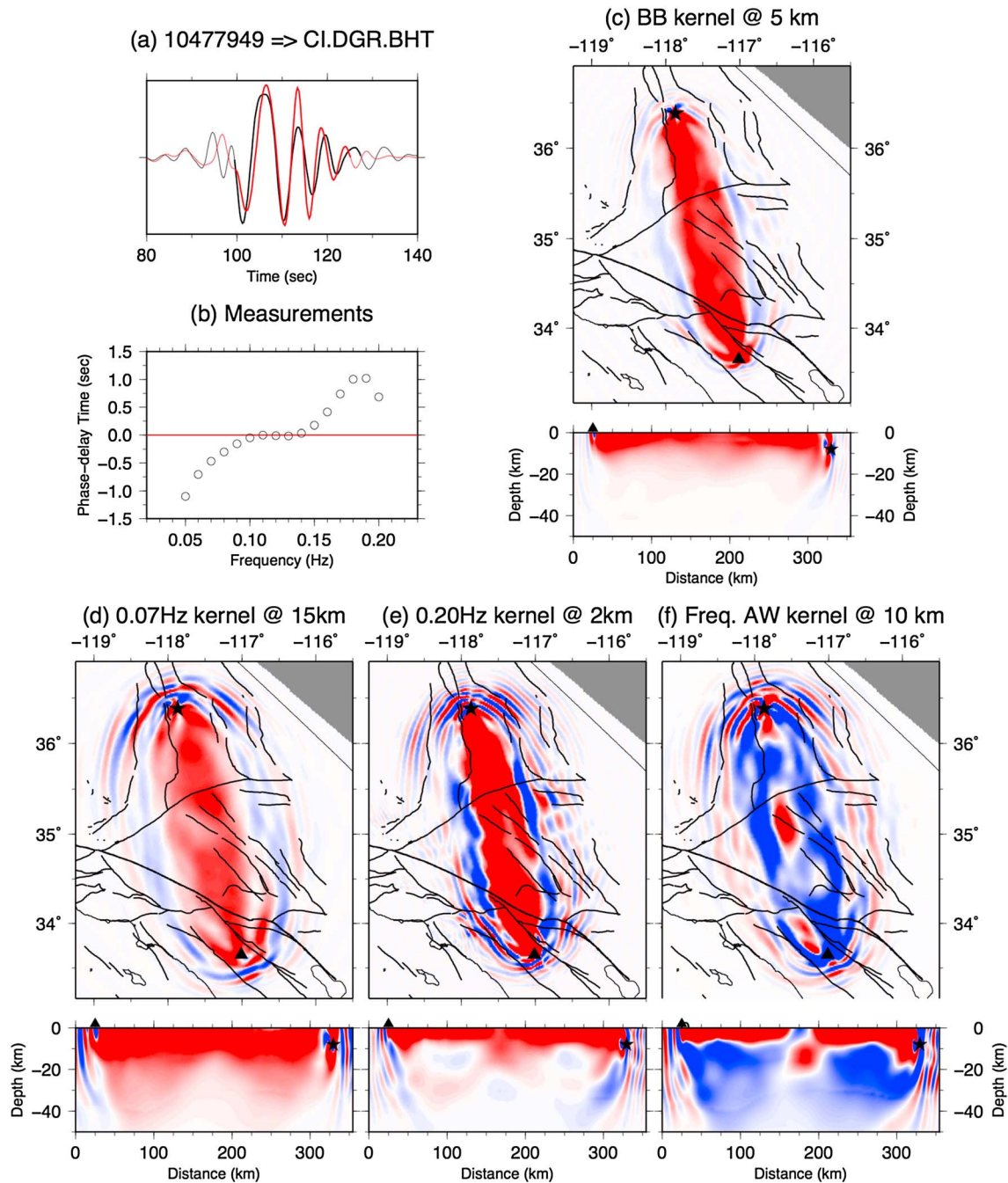
Figure D1. Examples of frequency-dependent data sensitivity kernels and the corresponding adjoint kernel for the waveforms shown in Figure A2. (a) Observed (black) and synthetic (red) waveforms; (b) broadband cross-correlation phase delay (red line) and frequency-dependent GSDF phase delay (black circles); (c) map view at (top) 5 km depth and (bottom) the cross-section view along the source-receiver path of the data sensitivity kernel for the broadband cross-correlation phase delay; (d, e) map view at 15 km and 2 km depths and cross-section view along the source-receiver path of the data sensitivity kernels for GSDF phase delay at 0.07 Hz and 0.2 Hz; (f) map view and cross-section view of the adjoint kernel, which is the summation of the data sensitivity kernels weighted by their corresponding measurements shown in Figure D1b. Vertical exaggeration on cross-section views is 2. Red indicates negative sensitivity (i.e., an increase in the velocity will result in a reduction in the misfit measurement) and blue indicates positive sensitivity.

in memory and all the data sensitivity kernels involving that RSGT were computed by reading the source-side strain fields back from the disk and performing the scattering integral. Once the data sensitivity kernels for all earthquakes were completed, the source-side strain fields were all deleted from the disk. The peak disk storage for one SI iteration was therefore around 39 Tb.
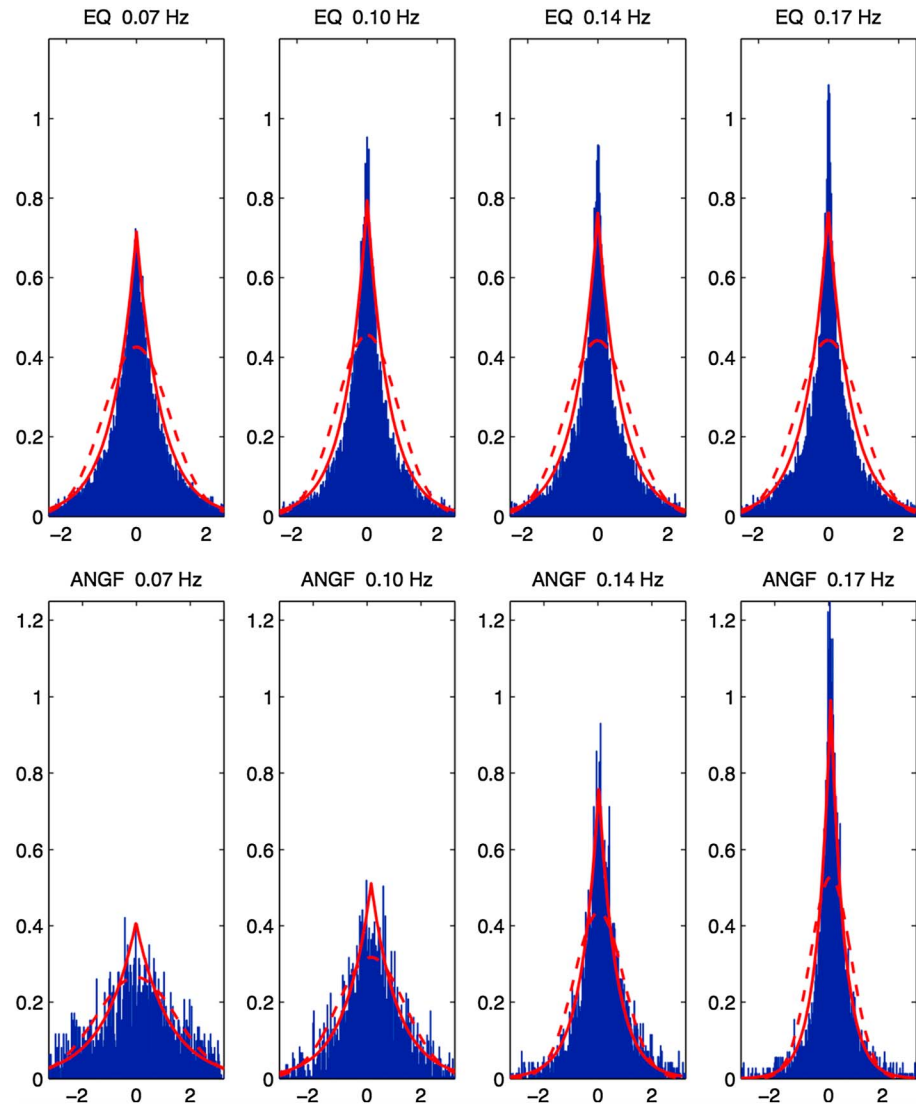
Figure E1. Distributions of errors for (top) frequency-dependent GSDF phase delay measured on earthquake waveform and (bottom) Rayleigh waves on ambient-noise correlograms at 0.07 Hz, 0.1 Hz, 0.14 Hz, and 0.17 Hz. Red solid lines: best fit Laplacian distributions; red dash lines: best fit normal distributions.

The data sensitivity kernels and the Jacobian matrix were stored in the compressed-sparse-column format [e.g., *Bai et al.*, 2000], and the disk space needed for storing the Jacobian consisting of more than 0.5 million data sensitivity kernels in our last SI iteration was around 7 Tb. Once the Jacobian matrix was constructed, the solution of the Gauss-Newton normal equation was then obtained by solving equation (8) using the optimized LSQR algorithm [*Lee et al.*, 2013]. Following *Chen et al.* [2007b], the "roughing operator" $\mathbf{C}_m^{-1/2}$ was chosen to be a linear combination of the identity operator and the Laplacian operator. The LSQR solver was run for a number of times for different damping coefficients, and the optimal damping coefficients were picked based on the L curve method. An optional line-search step could also be performed along the descent direction given by the LSQR solution.

Appendix D: Data Sensitivity Kernels

The SI method in *Zhao et al.* [2005, 2006] was derived for broadband cross-correlation traveltime delays and broadband cross-correlation amplitude ratios. To extend the same algorithm to a more general definition of
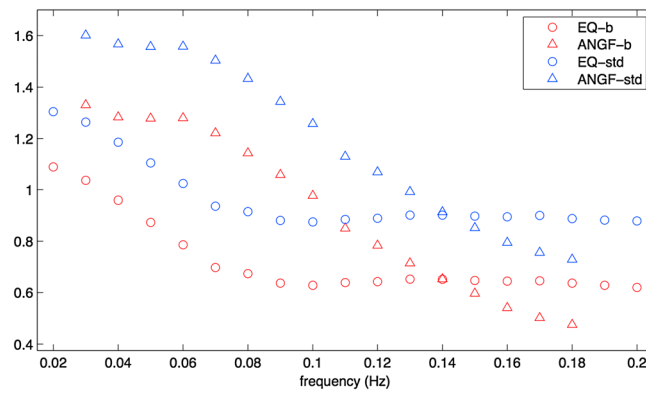
Figure E2. Frequency dependence of the standard deviation (blue) and the diversity (red) of the best fit normal and Laplacian distributions for errors of measurements made on earthquake waveforms (circles) and Rayleigh waves on ambient-noise correlagrams (triangles).

misfits, we introduced the concept of a *seismogram perturbation kernel* (SPK), which is the Fréchet derivative of the misfit measurement with respect to the synthetic waveform [*Chen et al.*, 2007a; *Chen*, 2011; *Liu and Gu*, 2012]:

$$\delta\mathrm{d} = \int J(t)\delta u(t)\mathrm{d}t$$

where $J(t)$ is the SPK and $u(t)$ is the synthetic seismogram. For the broadband cross-correlation traveltime delay, the SPK is the negative of the energy-normalized synthetic particle-velocity seismogram within the specified time window [*Luo and Schuster*, 1991; *Tanimoto*, 1995; *Zhao and Jordan*, 1998; *Dahlen et al.*, 2000;

Chen et al., 2007a]. For the frequency-dependent GSDF phase delay, the SPK, $J_p(t,\omega)$, where ω is the angular frequency at which the narrowband phase-delay misfit was measured, was derived in *Chen et al.* [2010]. The SPK for the frequency-dependent GSDF group delay $J_g(t,\omega)$ can be approximated by numerically differentiating $\omega J_p(t,\omega)$ with respect to ω using

$$J_g(t,\omega) \approx \left[(\omega + \Delta\omega)J_p(t,\omega + \Delta\omega) - \omega J_p(t,\omega)\right]/\Delta\omega$$

where $\Delta\omega$ is a sufficiently small frequency interval. Once the SPK is available, the data sensitivity kernel for the misfit can be computed by multiplying the space- and time-dependent Born kernel [e.g., *Dahlen and Tromp*, 1998; *Zhao et al.*, 2000] with the SPK and then integrating over time at every spatial grid point [*Chen et al.*, 2007a]. The adjoint source field for a seismic source can be obtained by multiplying all the SPKs associated with the seismic source with their corresponding misfit measurements, reversing the time axis and positioning them at their corresponding receiver locations [*Chen et al.*, 2007a]. The adjoint kernel of a seismic source obtained by computing the zero-lag temporal correlation between the adjoint wavefield and the time-reversed forward wavefield is a misfit-weighted summation of all the data sensitivity kernels associated with that seismic source [*Tromp et al.*, 2005; *Chen et al.*, 2007a].

Examples of the data sensitivity kernels for the broadband cross-correlation traveltime delay and the frequency-dependent GSDF phase delay computed using the SI method and the corresponding adjoint kernel computed using the AW method are shown in Figure D1. At lower frequencies, the data sensitivity kernels have wider first Fresnel zones and higher sensitivities at larger depths. The adjoint kernel is the misfit-weighted summation of the data sensitivity kernels at all frequencies. At lower frequencies, the GSDF phase-delay misfits are negative and the adjoint kernel at larger depths is positive, indicating that the reference *S* wave velocity is too slow at those depths. At higher frequencies, the GSDF phase-delay misfits are positive and the adjoint kernel at shallower depths is negative, indicating that the reference *S* wave velocity is too fast at those depths. The broadband cross-correlation traveltime delay for this example is nearly zero, and the corresponding adjoint kernel also has nearly zero amplitude throughout the region. The use of the frequency-dependent GSDF misfits can therefore substantially improve the resolution of our inversion.

Appendix E: Noise Model

For each GSDF phase-delay measurement we can estimate its measurement error using the SPK:

$$e(\omega) = \int J_p(t,\omega)q(t)\mathrm{d}t$$

where $q(t)$ is our estimate of the noise in the observed seismogram. For an earthquake recording, we estimate the seismogram noise using a segment of the seismogram within the time window $[t_0 - T, t_0)$, where t_0 is the time of the first break of the first arrival on the earthquake recording and T is set to 100 s in our study. For an ambient-noise correlagram, we estimated the noise by subtracting the correlagram obtained using 2 years of noise recordings from the correlagram obtained using 9 months of noise recordings. Histograms for the
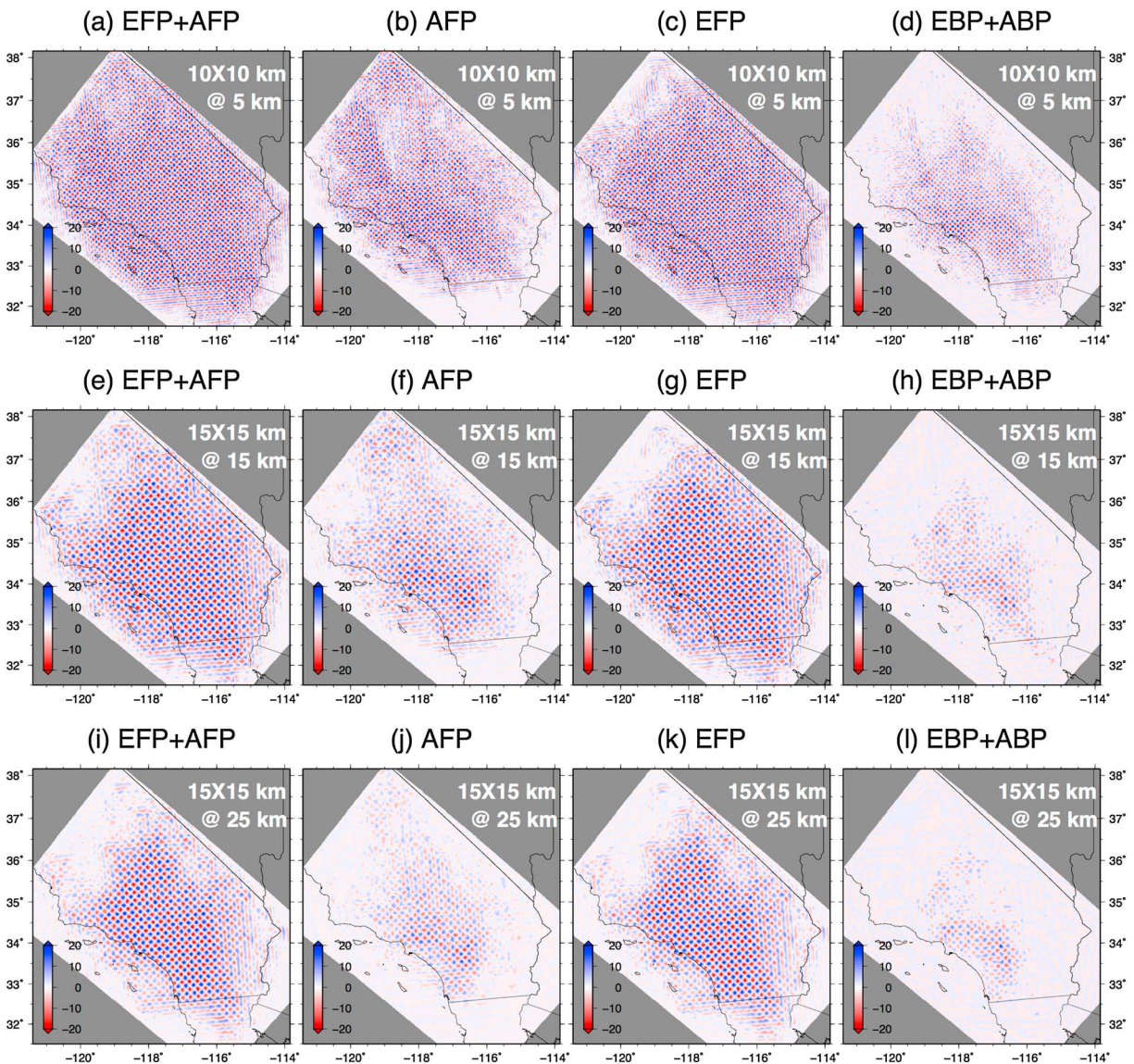
Figure F1. Recovered checkerboards at (a–d) 5 km, (e–h) 15 km, and (i–l) 25 km depths computed using the Jacobian of frequency-dependent GSDF phase delay measured on both earthquake waveforms (EFP) and ambient-noise correlagrams (AFP) (first column), the Jacobian of GSDF phase-delay measured only on ambient-noise correlagrams (second column), the Jacobian of GSDF phase-delay measured only on earthquake waveforms (third column), and the Jacobien of broadband cross-correlation phase-delay measured on both earthquake waveforms (EBP) and ambient-noise correlagrams (ABP) (fourth column). The size of the checker is 10 km by 10 km at 5 km depth and 15 km by 15 km at 15 km and 25 km depths.

estimated measurement errors of the GSDF phase-delay misfits measured at four different frequencies for earthquake recordings and ambient-noise correlagrams are shown in Figure E1. The histograms are better modeled using Laplace's first law of errors, which is known as the Laplacian or the double-exponential distribution, than using Laplace's second law of errors, better known as the Gaussian or normal distribution. Both the mean and the median of the histograms are very close to zero for all frequencies.

In Figure E2, we show the frequency dependence of the measurement errors. For earthquake recordings, the increase in the standard deviation and the diversity at frequencies below 0.08 Hz is likely due to the reduced signal-to-noise ratio at those frequencies. The standard deviation curves for earthquake recordings and ambient-noise Green's functions cross each other at ~0.14 Hz, which happens to be around the peak of the amplitude spectrum associated with the primary microseisms. The same is true for the two diversity curves. Below ~0.14 Hz, the standard deviation (diversity) of measurement errors for ambient-noise Green's functions increases with period faster than that for earthquake recordings, which may suggest a compound effect of

reduced signal-to-noise ratio, reduced randomness of the noise sources, and/or slower convergence toward the true Green's function, at those frequencies. At frequencies higher than ~0.14 Hz, the standard deviation (diversity) of measurement error in ambient-noise Green's functions reduces with frequency faster than that for earthquake recordings, which may suggest increased randomness of the noise sources and/or faster convergence toward the true Green's function at those frequencies [e.g., *Snieder*, 2004; *Kimman and Trampert*, 2010].

Appendix F: Resolution Analysis

In our checkerboard tests, the model perturbation $\Delta\mathbf{m}_k$ was chosen to be 3-D checkerboards with different checker sizes and we computed the synthetic data using the left-hand side of equation (8). Those synthetic data were then inverted by solving equation (8) using our LSQR solver. The differences between the recovered model and the input model depend upon the characteristics of the approximate Hessian, which were mainly determined by the source-receiver geometry, the waveforms used in the inversion, and the data sensitivity kernels for the misfit measurements made on those waveforms. For comparison, we also computed the data sensitivity kernels for broadband cross-correlation traveltime delays for all the waveforms used in our last SI iteration. Figure F1 shows the recovered checkerboards at different depths computed using the Jacobian of frequency-dependent GSDF phase-delay misfits and the Jacobian of broadband cross-correlation traveltime delays for earthquake seismograms only, the ambient-noise correlagrams only, and for the two data types combined. The use of the frequency-dependent GSDF misfits can significantly improve the resolution of the recovered model, especially at middle to lower crustal depths. The use of the ambient-noise correlagrams significantly improved the source-receiver path coverage, especially in the SSJB, the Sierra Nevada, and the Basin and Range provinces, where the number of earthquake seismograms is relatively low.

References

Akcelik, V., G. Biros, and O. Ghattas (2002), Parallel multiscale Gauss-Newton-Krylov methods for inverse wave propagation, in *Supercomputing, ACM/IEEE 2002 Conference*, pp. 41–41, IEEE, Baltimore, Md.

Akcelik, V., et al. (2003), High resolution forward and inverse earthquake modeling on terascale computers, in *Supercomputing, 2003 ACM/IEEE Conference*, pp. 52–52, ACM/IEEE, Phoenix, Ariz.

Aki, K., and P. G. Richards (2002), *Quantitative Seismology*, 2nd ed., Univ. Science Books, San Francisco, Calif.

Bai, Z., J. Demmel, J. Dongarra, A. Ruhe, and H. van der Vorst (2000), *Templates for the Solution of Algebraic Eigenvalue Problems: A Practical Guide*, 1st ed., Society for Industrial and Applied Mathematics, Philadelphia, Pa.

Bailey, E. H. (1941), *Mineralogy, Petrology and Geology of Santa Catalina Island*, Stanford Univ., Stanford, Calif.

Bailey, E. H., M. C. Blake Jr., and D. L. Jones (1970), On-land Mesozoic oceanic crust in California coast ranges, *U.S. Geol. Surv. Prof. Pap.*, *700*, C70–C81.

Balay, S., W. D. Gropp, L. C. McInnes, and B. F. Smith (1997), Efficient management of parallelism in object-oriented numerical software libraries, in *Modern Software Tools for Scientific Computing*, edited by E. Arge, A. M. Bruaset, and H. P. Langtangen, pp. 163–202, Birkhäuser, Boston, Mass.

Ben Hadj Ali, H., S. Operto, J. Virieux, and F. Sourbier (2009a), Efficient 3D frequency-domain full waveform inversion with phase encodings, in *71st Conference and Technical Exhibition*, p. 5812, EAGE, Extended Abstracts, Amsterdam, Netherlands.

Ben Hadj Ali, H., S. Operto, J. Virieux, and F. Sourbier (2009b), Three-dimensional frequency-domain full-waveform inversion with phase encoding, in *79th Annual International Meeting*, pp. 2288–2292, SEG, Extended Abstracts, Amsterdam, Netherlands.

Burchfiel, B. C., D. S. Cowan, and G. A. Davis (1992), Tectonic overview of the Cordilleran orogen in the western United States in The Geology of North America, G3, in *The Cordilleran Orogen: Conterminous United States BC Burchfiel*, edited by P. W. Lipman and M. L. Zoback, pp. 407–479, Geol. Soc. of Am., Boulder, Colo.

Carena, S., and J. Suppe (2002), Three-dimensional imaging of active structures using earthquake aftershocks: The Northridge thrust, California, *J. Struct. Geol.*, *24*(4), 887–904.

Chen, P. (2011), Full-wave seismic data assimilation: Theoretical background and recent advances, *Pure Appl. Geophys.*, *168*(10), 1527–1552.

Chen, P., T. H. Jordan, and L. Zhao (2007a), Full three-dimensional tomography: A comparison between the scattering-integral and adjoint-wavefield methods, *Geophys. J. Int.*, *170*(1), 175–181, doi:10.1111/j.1365-246X.2007.03429.x.

Chen, P., L. Zhao, and T. H. Jordan (2007b), Full 3D tomography for the crustal structure of the Los Angeles region, *Bull. Seismol. Soc. Am.*, *97*(4), 1094–1120, doi:10.1785/0120060222.

Chen, P., T. H. Jordan, and E.-J. Lee (2010), Perturbation kernels for generalized seismological data functionals (GSDF), *Geophys. J. Int.*, *183*(2), 869–883, doi:10.1111/j.1365-246X.2010.04758.x.

Christensen, N. I., and W. D. Mooney (1995), Seismic velocity structure and composition of the continental crust: A global view, *J. Geophys. Res.*, *100*(B6), 9761–9788, doi:10.1029/95JB00259.

Clemens-Knott, D., and J. B. Saleeby (1999), Impinging ring dike complexes in the Sierra Nevada batholith, California: Roots of the Early Cretaceous volcanic arc, *Geol. Soc. Am. Bull.*, *111*(4), 484–496, doi:10.1130/0016-7606(1999)111<0484:IRDCIT>2.3.CO;2.

Clemens-Knott, D., M. B. Wolf, and J. B. Saleeby (2000), Middle Mesozoic plutonism and deformation in the western Sierra Nevada foothills, California, *Geol. Soc. Am. Field Guide*, *2*, 205–221.

Colli, L., A. Fichtner, and H. P. Bunge (2013), Full waveform tomography of the upper mantle in the South Atlantic region: Imaging a westward fluxing shallow asthenosphere, *Tectonophysics*, *604*, 26–40, doi:10.1016/j.tecto.2013.06.015.

Cui, Y., R. Moore, K. Olsen, A. Chourasia, P. Maechling, B. Minster, S. Day, Y. Hu, J. Zhu, and T. Jordan (2009), Toward petascale earthquake simulations, *Acta Geotech.*, *4*(2), 79–93, doi:10.1007/s11440-008-0055-2.

Cui, Y., et al. (2010), Scalable earthquake simulation on petascale supercomputers, in *High Performance Computing, Networking, Storage and Analysis (SC), 2010 International Conference for*, pp. 1–20, ACM Gordon Bell Finalist, New Orleans, La.

Dahlen, F. A., and J. Tromp (1998), *Theoretical Global Seismology*, Princeton Univ. Press, Princeton, N. J.

Dahlen, F. A., S. H. Hung, and G. Nolet (2000), Fréchet kernels for finite-frequency traveltimes, *Geophys. J. Int.*, *141*, 157–174.

Davis, T. L., M. B. Lagoe, W. J. M. Bazeley, S. Gordon, K. McIntosh, and J. S. Namson (1988), Structure of the Cuyama Valley, Caliente Range, and Carrizo Plain and its significance to the structural style of the southern Coast Ranges and western Transverse Ranges, pp. 141–158.

Derode, A., E. Larose, M. Tanter, J. de Rosny, A. Tourin, M. Campillo, and M. Fink (2003), Recovering the Green's function from field-field correlations in an open scattering medium (L), *J. Acoust. Soc. Am.*, *113*(6), 2973.

Ducea, M. N., S. Kidder, J. T. Chesley, and J. B. Saleeby (2009), Tectonic underplating of trench sediments beneath magmatic arcs: The central California example, *Int. Geol. Rev.*, *51*(1), 1–26, doi:10.1080/00206810802602767.

Ely, G. P., T. H. Jordan, P. Small, and P. J. Maechling (2010), A Vs 30-derived near-surface seismic velocity model, in *Abstract S51A-1907*, *Fall Meeting*.

Ernst, W. G. (1981), *The Geotectonic Development of California*, 706 pp., Prentice Hall, Englewood Cliffs, N. J.

Fichtner, A. (2011), *Full Seismic Waveform Modelling and Inversion*, Springer, Berlin/Heidelberg, Germany.

Fichtner, A. (2014), Source and processing effects on noise correlations, *Geophs. J. Int.*, doi:10.1093/gji/ggu093.

Fichtner, A., B. L. N. Kennett, H. Igel, and H.-P. Bunge (2009), Full seismic waveform tomography for upper-mantle structure in the Australasian region using adjoint methods, *Geophys. J. Int.*, *179*(3), 1703–1725, doi:10.1111/j.1365-246X.2009.04368.x.

Fichtner, A., E. Saygin, T. Taymaz, P. Cupillard, Y. Capdeville, and J. Trampert (2013), The deep structure of the North Anatolian Fault Zone, *Earth Planet. Sci. Lett.*, *373*, 109–117.

Fliedner, M. M., S. L. Klemperer, and N. I. Christensen (2000), Three-dimensional seismic model of the Sierra Nevada arc, California, and its implications for crustal and upper mantle composition, *J. Geophys. Res.*, *105*(B5), 10,899–10,921, doi:10.1029/2000JB900029.

French, S. W., V. Lekic, and B. Romanowicz (2013), Waveform tomography reveals channeled flow at the base of the oceanic asthenosphere, *Science*, *342*, 227–230.

Fuis, G., et al. (2012), Investigating earthquake hazards in the Northern Salton Trough, Southern California, Using Data From the Salton Seismic Imaging Project (SSIP), *AGU Fall Meet. Abstr.*, −1, 06.

Fuis, G. S., et al. (2003), Fault systems of the 1971 San Fernando and 1994 Northridge earthquakes, southern California: Relocated aftershocks and seismic images from LARSE II, *Geology*, *31*(2), 171, doi:10.1130/0091-7613(2003)031<0171:FSOTSF>2.0.CO;2.

Gee, L. S., and T. H. Jordan (1992), Generalized seismological data functionals, *Geophys. J. Int.*, *111*(2), 363–390.

Gilbert, H., C. Jones, T. J. Owens, and G. Zandt (2007), Imaging Sierra Nevada lithospheric sinking, *Eos Trans. AGU*, *88*(21), 225–229, doi:10.1029/2007EO210001.

Godfrey, N. J., and S. L. Klemperer (1998), Ophiolitic basement to a forearc basin and implications for continental growth: The Coast Range/Great Valley ophiolite, California, *Tectonics*, *17*(4), 558–570, doi:10.1029/98TC01536.

Graves, R., et al. (2010), CyberShake: A physics-based seismic hazard model for Southern California, *Pure Appl. Geophys.*, *168*(3–4), 367–381, doi:10.1007/s00024-010-0161-6.

Hadley, D., and H. Kanamori (1977), Seismic structure of the Transverse Ranges, California, *Geol. Soc. Am. Bull.*, *88*(10), 1469–1478, doi:10.1130/0016-7606(1977)88<1469:SSOTTR>2.0.CO;2.

Hall, C. A., Jr. (1991), *Geology of the Point Sur-Lopez Point Region, Coast Ranges, California: A Part of the Southern California Allochthon*, p. 40, Geol. Soc. of Am. (GSA), Boulder, Colo.

Han, L., J. A. Hole, J. M. Stock, G. S. Fuis, N. W. Driscoll, A. M. Kell, G. Kent, A. J. Harding, A. Gonzalez-Fernandez, and O. Lazaro-Mancilla (2013), Crustal structure during active rifting in the central Salton Trough, California, constrained by the Salton Seismic Imaging Project (SSIP), *AGU Fall Meet. Abstr.*, −1, 2478.

Hauksson, E. (2000), Crustal structure and seismicity distribution adjacent to the Pacific and North America plate boundary in southern California, *J. Geophys. Res.*, *105*(B6), 13,875–13,903, doi:10.1029/2000JB900016.

Hauksson, E., et al. (2001), Southern California Seismic Network: Caltech/USGS Element of TriNet 1997–2001, *Seismol. Res. Lett.*, *72*(6), 690–704.

Hoaglin, D. C., F. Mosteller, and J. W. Tukey (1983), *Understanding Robust and Exploratory Data Analysis*, pp. 404–414, John Wiley.

Ingersoll, R. V. (1982), Initiation and evolution of the Great Valley forearc basin of northern and central California, U.S.A., *Geol. Soc. Lond. Spec. Publ.*, *10*(1), 459–467, doi:10.1144/GSL.SP.1982.010.01.31.

Jennings, C. W. (1977), Geologic map of California: California Division of Mines and Geology, Geologic Data Map Series, Mpa 2, scale 1:750,000.

Katzman, R., L. Zhao, and T. H. Jordan (1998), High-resolution, two-dimensional vertical tomography of the central Pacific mantle using ScS reverberations and frequency-dependent travel times, *J. Geophys. Res.*, *103*(B8), 17,933–17,971, doi:10.1029/98JB00504.

Keller, M. A. (1990), Introduction to stratigraphy and hydrocarbon occurrence in Oligocene and Miocene rocks of the Santa Barbara-Ventura and Santa Maria basins of California, in *Miocene and Oligocene Petroleum Reservoirs of the Santa Maria and Santa Barbara-Ventura Basins*, edited by M. A. Keller and M. K. McGowen, compilers, pp. 1–11, California: A core workshop: SEPM (Society for Sedimentary Geology) Core Workshop 14, San Francisco, Calif.

Kimman, W. P., and J. Trampert (2010), Approximations in seismic interferometry and their effects on surface waves, *Geophys. J. Int.*, *182*(1), 461–476.

Kohler, M. D., H. Magistrale, and R. W. Clayton (2003), Mantle heterogeneities and the SCEC reference three-dimensional seismic velocity model version 3, *Bull. Seismol. Soc. Am.*, *93*(2), 757–774, doi:10.1785/0120020017.

Komatitsch, D., and J. Tromp (1999), Introduction to the spectral element method for three-dimensional seismic wave propagation, *Geophys. J. Int.*, *139*(3), 806–822, doi:10.1046/j.1365-246x.1999.00967.x.

Kustowski, B., G. Ekström, and A. M. Dziewonski (2008), Anisotropic shear-wave velocity structure of the Earth's mantle: A global model, *J. Geophys. Res.*, *113*, B06306, doi:10.1029/2007JB005169.

Lawrence, J. F., and G. A. Prieto (2011), Attenuation tomography in the western United States from ambient seismic noise, *J. Geophys. Res.*, *116*, B06302, doi:10.1029/2010JB007836.

Lee, E., P. Chen, and T. H. Jordan (2014), Testing waveform predictions of 3D velocity models against two recent Los Angeles earthquakes, *Seismol. Res. Lett.*, *85*(6), 1–11.

Lee, E.-J., and P. Chen (2013), Automating seismic waveform analysis for full 3-D waveform inversions, *Geophys. J. Int.*, *194*(1), 572–589, doi:10.1093/gji/ggt124.

Lee, E.-J., P. Chen, T. H. Jordan, and L. Wang (2011), Rapid full-wave centroid moment tensor (CMT) inversion in a three-dimensional earth structure model for earthquakes in Southern California, *Geophys. J. Int.*, *186*(1), 311–330, doi:10.1111/j.1365-246X.2011.05031.x.

Lee, E.-J., H. Huang, J. M. Dennis, P. Chen, and L. Wang (2013), An optimized parallel LSQR algorithm for seismic tomography, *Comput. Geosci.*, *61*, 184–197, doi:10.1016/j.cageo.2013.08.013.

Legg, M. R. (1991), Developments in understanding the tectonic evolution of the California Continental Borderland, in *From Shoreline to Abyss*, vol. 46, edited by R. H. Osborne, pp. 291–312, Society of Economic Paleontologists and Mineralogists Special Publication, Tulsa, Okla.

Lekic, V., and B. Romanowicz (2011), Inferring upper-mantle structure by full waveform tomography with the spectral- element method, *Geophys. J. Int.*, *185*, 799–831.

Liu, Q., and Y. J. Gu (2012), Seismic imaging: From classical to adjoint tomography, *Tectonophysics*, *566–567*, 31–66, doi:10.1016/j.tecto.2012.07.006.

Liu, Q., and J. Tromp (2006), Finite-frequency kernels based on adjoint methods, *Bull. Seismol. Soc. Am.*, *96*(6), 2383–2397, doi:10.1785/0120060041.

Livers, A. J., L. Han, J. Delph, A. White-Gaynor, R. Petit, J. A. Hole, J. M. Stock, and G. S. Fuis (2012), Tomographic characteristics of the northern geothermally active rift zone of the Imperial Valley and its rift margins: Salton Seismic Imaging Project (SSIP), *AGU Fall Meet. Abstr.*

Lobkis, O. I., and R. L. Weaver (2001), On the emergence of the Green's function in the correlations of a diffuse field, *J. Acoust. Soc. Am.*, *110*(6), 3011.

Luo, Y., and G. T. Schuster (1991), Wave-equation traveltime inversion, *Geophysics*, *56*(5), 645–653.

Lutter, W. J., G. S. Fuis, C. H. Thurber, and J. Murphy (1999), Tomographic images of the upper crust from the Los Angeles basin to the Mojave Desert, California: Results from the Los Angeles region seismic experiment, *J. Geophys. Res.*, *104*(B11), 25,543–25,565, doi:10.1029/1999JB900188.

Lutter, W. J., G. S. Fuis, T. Ryberg, D. A. Okaya, R. W. Clayton, P. M. Davis, C. Prodehl, J. M. Murphy, V. E. Langenheim, and M. L. Benthien (2004), Upper crustal structure from the Santa Monica mountains to the Sierra Nevada, southern California: Tomographic results from the Los Angeles regional seismic experiment, Phase II (LARSE II), *Bull. Seismol. Soc. Am.*, *94*(2), 619–632.

Ma, S., G. A. Prieto, and G. C. Beroza (2008), Testing community velocity models for Southern California using the ambient seismic field, *Bull. Seismol. Soc. Am.*, *98*(6), 2694–2714, doi:10.1785/0120080947.

Mack, S., J. B. Saleeby, and J. E. Farrell (1979), Origin and emplacement of the Academy Pluton Fresno County, California, *Geol. Soc. Am. Bull.*, *90*, 633–694.

Magistrale, H., K. McLaughlin, and S. Day (1996), A geology-based 3D velocity model of the Los Angeles basin sediments, *Bull. Seismol. Soc. Am.*, *86*(4), 1161–1166.

Magistrale, H., S. Day, R. W. Clayton, and R. Graves (2000), The SCEC Southern California reference three-dimensional seismic velocity model version 2, *Bull. Seismol. Soc. Am.*, *90*(6B), S65–S76, doi:10.1785/0120000510.

Marcinkovich, C., and K. B. Olsen (2003), On the implementation of perfectly matched layers in a three-dimensional fourth-order velocity-stress finite difference scheme, *J. Geophys. Res.*, *108*(B5), 2276, doi:10.1029/2002JB002235.

Nocedal, J., and S. Wright (2006), *Numerical Optimization*, 686 pp., Springer Science & Business Media, New York.

Olsen, K. B. (1994), Simulation of three-dimensional wave propagation in the Salt Lake Basin, PhD thesis, Univ. of Utah, Salt Lake City, Utah.

Olsen, K. B., J. C. Pechmann, and G. T. Schuster (1995), Simulation of 3D elastic wave propagation in the Salt Lake Basin, *Bull. Seismol. Soc. Am.*, *85*(6), 1688–1710.

Pellerin, C. L. M., and N. I. Christensen (1998), Interpretation of crustal seismic velocities in the San Gabriel—Mojave region, southern California, *Tectonophysics*, *286*(1), 253–271.

Peter, D., et al. (2011), Forward and adjoint simulations of seismic wave propagation on fully unstructured hexahedral meshes, *Geophys. J. Int.*, *186*(2), 721–739, doi:10.1111/j.1365-246X.2011.05044.x.

Platt, J. P. (1975), Metamorphic and deformational processes in the Franciscan Complex, California: Some insights from the Catalina Schist terrane, *Geol. Soc. Am. Bull.*, *86*(10), 1337–1347, doi:10.1130/0016-7606(1975)86<1337:MADPIT>2.0.CO;2.

Plesch, A., et al. (2007), Community Fault Model (CFM) for Southern California, *Bull. Seismol. Soc. Am.*, *97*(6), 1793–1802, doi:10.1785/0120050211.

Plesch, A., C. Tape, R. Graves, J. H. Shaw, P. Small, and G. P. Ely (2011), Updates for the CVM-H including new representations of the offshare Santa Maria and San Bernardino basin and a new Moho surface, in *2011 Southern California Earthquake Center Annual Meeting, Proceedings and Abstracts*, vol. 21, p. 137, Southern California Earthquake Center, Palm Springs, Calif.

Porter, R., G. Zandt, and N. McQuarrie (2011), Pervasive lower-crustal seismic anisotropy in Southern California: Evidence for underplated schists and active tectonics, *Lithosphere*, *3*(3), 201–220, doi:10.1130/L126.1.

Pratt, R. G. (1990), Frequency-domain elastic wave modeling by finite differences: A tool for crosshole seismic imaging, *Geophysics*, *55*(5), 626–632, doi:10.1190/1.1442874.

Pratt, R. G., C. Shin, and G. J. Hicks (1998), Gauss-Newton and full Newton methods in frequency-space seismic waveform inversion, *Geophys. J. Int.*, *133*, 341–362.

Press, W. H., S. A. Teukolsky, W. T. Vetterling, and B. P. Flannery (1992), *Numerical Recipes in C, the Art of Scientific Computing*, Cambridge Univ. Press, New York.

Prieto, G. A., J. F. Lawrence, G. C. Beroza (2009), Anelastic Earth structure from the coherency of the ambient seismic field, *J. Geophys. Res.*, *114*, B07303, doi:10.1029/2008JB006067.

Prieto, G. N. A., M. Denolle, J. F. Lawrence, and G. C. Beroza (2011), On amplitude information carried by the ambient seismic field, *C. R. Geosci.*, *343*(8–9), 600–614, doi:10.1016/j.crte.2011.03.006.

Prieux, V., R. Brossier, S. Operto, and J. Virieux (2013), Multiparameter full waveform inversion of multicomponent ocean- bottom-cable data from the Valhall field. Part 1: Imaging compressional wave speed, density and attenuation, *194*(3), 1640–1664, *Geophys. J. Int.*, doi:10.1093/gji/ggt177.

Prindle, K., and T. Tanimoto (2006), Teleseismic surface wave study for S-wave velocity structure under an array: Southern California, *Geophys. J. Int.*, *166*(2), 601–621.

Rickett, J., and J. Claerbout (1999), Acoustic daylight imaging via spectral factorization: Helioseismology and reservoir monitoring, *Leading Edge*, *18*(8), 957–960.

Rose, E. J., et al. (2013), Borehole-explosion and air-gun data acquired in the 2011 Salton Seismic Imaging Project (SSIP), southern California —Description of the survey, *U.S. Geol. Surv. Open File Rep.*, *2013–1172*, 84 pp., doi:10.3133/ofr20131172.

Saleeby, J. (2003), Segmentation of the Laramide Slab—Evidence from the southern Sierra Nevada region, *Geol. Soc. Am. Bull.*, *115*(6), 655–668, doi:10.1130/0016-7606(2003)115<0655:SOTLSF>2.0.CO;2.

Saleeby, J., and W. Sharp (1980), Chronology of the structural and petrologic development of the southwest Sierra Nevada foothills, California: Summary, *Geol. Soc. Am. Bull.*, *91*(6), 317–320, doi:10.1130/0016-7606(1980)91<317:COTSAP>2.0.CO;2.

Saleeby, J., M. Ducea, and D. Clemens-Knott (2003), Production and loss of high-density batholithic root, southern Sierra Nevada, California: High-density batholithic root, *Tectonics*, *22*(6), 1064, doi:10.1029/2002TC001374.

Schaeffer A. J., and S. Lebedev (2014), Imaging the North American continent using waveform inversion of global and USArray data, *Earth Planet. Sci. Lett.*, doi:10.1016/j.epsl.2014.05.014, in press.

Schiemenz, A., and H. Igel (2013), Accelerated 3-D full-waveform inversion using simultaneously encoded sources in the time domain: Application to Valhall ocean-bottom cable data, *Geophs. J. Int.*, *195*, 1970–1988.

Sipkin, S. A., and T. H. Jordan (1980), Multiple ScS travel times in the western Pacific: Implications for mantle heterogeneity, *J. Geophys. Res.*, *85*(B2), 853–861, doi:10.1029/JB085iB02p00853.

Snieder, R. (2004), Extracting the Green's function from the correlation of coda waves: A derivation based on stationary phase, *Phys. Rev. E*, *69*(4), 046610, doi:10.1103/PhysRevE.69.046610.

Snieder, R., K. Wapenaar, and U. Wegler (2007), Unified Green's function retrieval by cross-correlation; Connection with energy principles, *Phys. Rev. E*, *75*(3), doi:10.1103/PhysRevE.75.036103.

Stehly, L., M. Campillo, and N. M. Shapiro (2006), A study of the seismic noise from its long-range correlation properties, *J. Geophys. Res.*, *111*, B10306, doi:10.1029/2005JB004237.

Süss, M. P., and J. H. Shaw (2003), P wave seismic velocity structure derived from sonic logs and industry reflection data in the Los Angeles basin, California, *J. Geophys. Res.*, *108*(B3), 2170, doi:10.1029/2001JB001628.

Tanimoto, T. (1995), Formalism for traveltime inversion with finite frequency effects, *Geophys. J. Int.*, *121*(1), 103–110, doi:10.1111/j.1365-246X.1995.tb03513.x.

Tape, C., Q. Liu, and J. Tromp (2007), Finite-frequency tomography using adjoint methods—Methodology and examples using membrane surface waves, *Geophys. J. Int.*, *168*(3), 1105–1129, doi:10.1111/j.1365-246X.2006.03191.x.

Tape, C., Q. Liu, A. Maggi, and J. Tromp (2009), Adjoint tomography of the Southern California crust, *Science*, *325*(5943), 988–992, doi:10.1126/science.1175298.

Tape, C., Q. Liu, A. Maggi, and J. Tromp (2010), Seismic tomography of the southern California crust based on spectral-element and adjoint methods, *Geophys. J. Int.*, *180*(1), 433–462, doi:10.1111/j.1365-246X.2009.04429.x.

Tarantola, A. (1984), Inversion of seismic reflection data in the acoustic approximation, *Geophysics*, *49*(8), 1259–1266, doi:10.1190/1.1441754.

Tarantola, A. (1988), Theoretical background for the inversion of seismic waveforms including elasticity and attenuation, *Pure Appl. Geophys.*, *128*(1–2), 365–399, doi:10.1007/BF01772605.

Tromp, J., C. Tape, and Q. Liu (2005), Seismic tomography, adjoint methods, time reversal and banana-doughnut kernels, *Geophys. J. Int.*, *160*(1), 195–216, doi:10.1111/j.1365-246X.2004.02453.x.

Tromp, J., Y. Luo, S. Hanasoge, and D. Peter (2010), Noise cross-correlation sensitivity kernels, *Geophys. J. Int.*, *183*(2), 791–819, doi:10.1111/j.1365-246X.2010.04721.x.

Tsai, V. C. (2011), Understanding the amplitudes of noise correlation measurements, *J. Geophys. Res.*, *116*, B09311, doi:10.1029/2011JB008483.

Wapenaar, K. (2004), Retrieving the elastodynamic Green's function of an arbitrary inhomogeneous medium by cross correlation, *Phys. Rev. Lett.*, *93*(25), doi:10.1103/PhysRevLett.93.254301.

Weaver, R. L., and O. I. Lobkis (2004), Diffuse fields in open systems and the emergence of the Green's function (L), *J. Acoust. Soc. Am.*, *116*(5), 2731, doi:10.1121/1.1810232.

Wessel, P., and W. H. F. Smith (1991), Free software helps map and display data, *Eos Trans. AGU*, *72*, 441–446, doi:10.1029/90EO00319.

Woodford, A. O. (1924), The Catalina metamorphic facies of the Franciscan series: University of California, *Dept. Geol. Sc. Bull.*, *15*(3), 49–68.

Xu, Z., P. Chen, and Y. Chen (2013), Sensitivity kernel for the weighted norm of the frequency-dependent phase correlation, *Pure Appl. Geophys.*, *170*(3), 353–371, doi:10.1007/s00024-012-0507-3.

Yan, Z., and R. W. Clayton (2007), Regional mapping of the crustal structure in southern California from receiver functions, *J. Geophys. Res.*, *112*, B05311, doi:10.1029/2006JB004622.

Zhao, L., and T. H. Jordan (1998), Sensitivity of frequency-dependent traveltimes to laterally heterogeneous, anisotropic Earth structure, *Geophys. J. Int.*, *133*(3), 683–704, doi:10.1046/j.1365-246X.1998.00524.x.

Zhao, L., T. H. Jordan, and C. H. Chapman (2000), Three-dimensional Fréchet differential kernels for seismic delay times, *Geophys. J. Int.*, *141*, 58–576.

Zhao, L., T. H. Jordan, K. B. Olsen, and P. Chen (2005), Fréchet kernels for imaging regional Earth structure based on three-dimensional reference models, *Bull. Seismol. Soc. Am.*, *95*(6), 2066–2080, doi:10.1785/0120050081.

Zhao, L., P. Chen, and T. H. Jordan (2006), Strain Green's tensors, reciprocity, and their applications to seismic source and structure studies, *Bull. Seismol. Soc. Am.*, *96*(5), 1753–1763, doi:10.1785/0120050253.

Zhu, H., E. Bozdağ, D. Peter, and J. Tromp (2012), Structure of the European upper mantle revealed by adjoint tomography, *Nat. Geosci.*, *5*(7), 493–498, doi:10.1038/ngeo1501.

Zhu, L., and D. V. Helmberger (1996), Advancement in source estimation techniques using broadband regional seismograms, *Bull. Seismol. Soc. Am.*, *86*(5), 1634–1641.

Zhu, L., and H. Kanamori (2000), Moho depth variation in southern California from teleseismic receiver functions, *J. Geophys. Res.*, *105*(B2), 2969–2980, doi:10.1029/1999JB900322.